eLife

Reviewed Preprint
v2 • August 7, 2024
Revised by authors

Reviewed Preprint
v1 • February 2, 2024

Neuroscience

A non-conducting role of the $Ca_V1.4$ Ca^{2+} channel drives homeostatic plasticity at the cone photoreceptor synapse

J Wesley Maddox, Gregory J Ordemann, Juan de la Rosa Vázquez, Angie Huang, Christof Gault, Serena R Wisner, Kate Randall, Daiki Futagi, Nihal A Salem, R Dayne Mayfield, Boris V Zemelman, Steven H DeVries, Mrinalini Hoon, Amy Lee

Dept of Neuroscience, University of Texas-Austin, Austin, TX 78712, USA • Dept. of Ophthalmology and Visual Sciences, University of Wisconsin-Madison, Madison, WI, 53706, USA • Neuroscience Training Program, University of Wisconsin-Madison, Madison WI 53706 USA • Dept. of Ophthalmology, Northwestern University Feinberg School of Medicine, Chicago, IL, 60611, USA • McPherson Eye Research Institute, Madison WI 53706 USA

Abstract

In congenital stationary night blindness type 2 (CSNB2)—a disorder involving the $Ca_V1.4$ (L-type) Ca^{2+} channel—visual impairment is mild considering that $Ca_V1.4$ mediates synaptic release from rod and cone photoreceptors. Here, we addressed this conundrum using a $Ca_V1.4$ knockout (KO) mouse and a knock-in (G369i KI) mouse expressing a non-conducting $Ca_V1.4$. Surprisingly, Ca_V3 (T-type) Ca^{2+} currents were detected in cones of G369i KI mice and $Ca_V1.4$ KO mice but not in cones of wild-type mouse, ground squirrel, and macaque retina. Whereas $Ca_V1.4$ KO mice are blind, G369i KI mice exhibit normal photopic (i.e., cone-mediated) visual behavior. Cone synapses, which fail to form in $Ca_V1.4$ KO mice, are present, albeit enlarged, and with some errors in postsynaptic wiring in G369i KI mice. While $Ca_V1.4$ KO mice lack evidence of cone synaptic responses, electrophysiological recordings in G369i KI mice revealed nominal transmission from cones to horizontal cells and bipolar cells. In CSNB2, we propose that Ca_V3 channels maintain cone synaptic output provided that the nonconducting role of $Ca_V1.4$ in cone synaptogenesis remains intact. Our findings reveal an unexpected form of homeostatic plasticity that relies on a non-canonical role of an ion channel.

eLife assessment

Based on analyses of retinae from genetically modified mice, and from wild-type ground squirrel and macaque, employing microscopic imaging, electrophysiology, and pharmacological manipulations, this **valuable** study on the role of Cav1.4 calcium channels in cone photoreceptor cells (i) shows that the expression of a Cav1.4 variant lacking calcium conductivity supports the development of cone synapses beyond what is observed in the complete absence of Cav1.4, and (ii) indicates that the cone pathway can partially operate even without calcium flux through Cav1.4 channels, thus preserving behavioral responses under bright light. The evidence for the function of Cav1.4 protein in synapse development is **convincing** and in agreement with a closely related earlier study by the same authors on rod photoreceptors. The mechanism of compensation of Cav1.4 loss by Cav3 remains unclear but appears to involve post-transcriptional processes. As congenital Cav1.4 dysfunction can cause stationary night blindness, this work relates to a wide range of neuroscience topics, from synapse biology to neuro-ophthalmology.

https://doi.org/10.7554/eLife.94908.2.sa2

Introduction

At the first synapse in the visual pathway, graded electrical signals produced in rod and cone photoreceptors gate the release of glutamate onto postsynaptic neurons. Photoreceptor synapses are specialized with a ribbon organelle, which helps prime synaptic vesicles, [1], [2] and postsynaptic neurites of horizontal and bipolar cells that invaginate deep within the terminal [3]. A variety of proteins interact with the ribbon and synaptic vesicles near release sites (*i.e.*, active zones) [4]. The importance of these proteins for vision is illustrated by the numerous inherited retinal diseases linked to mutations in their encoding genes [5].

One such gene is *CACNA1F*, which encodes the voltage-gated Ca^{2+} (Ca_V) channel expressed in retinal photoreceptors, $Ca_V1.4$ [6]–[8]. Among the sub-family of Ca_V1 L-type channels, $Ca_V1.4$ exhibits unusually slow inactivation that is well-matched for supporting the tonic, Ca^{2+}-dependent release of glutamate from photoreceptor synaptic terminals in darkness [9], [10]. More than 200 mutations in *CACNA1F* cause vision disorders including congenital stationary night blindness type 2 (CSNB2) [11], [12]. These mutations are broadly categorized as producing a gain of function or loss of function in $Ca_V1.4$ [13]. How these mutations in *CACNA1F* lead to the variable clinical phenotypes of CSNB2 is largely unknown. Symptoms may include strabismus, low visual acuity, and in many cases, night blindness [14], [15]. The latter suggests a primary defect in rod pathways, which is surprising given that $Ca_V1.4$ knockout (KO) mice are completely blind and lack any evidence of either rod or cone synaptic responses [6], [7], [16]. A major caveat is that rod and cone synapses do not form in $Ca_V1.4$ KO mice [7], [16]–[18]. Thus, $Ca_V1.4$ KO mice are not suitable for studies of how *CACNA1F* mutations differentially affect rod and cone pathways or for efforts to uncover how the biophysical properties of $Ca_V1.4$ shape photoreceptor synaptic release properties.

Here, we overcome this hurdle with a knock-in mouse strain (G369i KI) expressing a non-conducting mutant form of $Ca_V1.4$ [19]. We show that, although greatly impaired, cone synapses and downstream signaling through cone pathways can support photopic visual function in G369i KI mice. This novel mechanism requires the ability of the $Ca_V1.4$ protein, independent of its Ca^{2+} conductance, to nucleate the assembly of cone ribbon synapses and involves an aberrant Ca_V3 (T-type) conductance that appears when $Ca_V1.4$ Ca^{2+} signals are compromised.

Results

Cone pedicles and ribbons are present in G369i KI mice but not in $Ca_V1.4$ KO mice

The G369i mutation results in an insertion of a glycine residue in a transmembrane domain, which prevents Ca^{2+} permeation through $Ca_V1.4$[19]. The presence of rod synapses in G369i KI mice but not $Ca_V1.4$ KO mice indicates that the $Ca_V1.4$ protein and not its Ca^{2+} conductance is required for rod synapse assembly[19]. To test if this is also true for cones, we performed immunofluorescence and confocal analyses using antibodies against cone arrestin (CAR) and CtBP2 to label cone terminals (i.e., pedicles) and ribbons, respectively (**Fig. 1**). In $Ca_V1.4$ KO mouse retinas, cone pedicles were shrunken and retracted into the outer nuclear layer (ONL, **Fig. 1a**) with little evidence of elongated ribbons (**Fig. 1b**). In contrast, cone pedicles in G369i KI mice were normally localized in the outer plexiform layer (OPL, **Fig. 1a**) and were populated by multiple ribbons that were associated with labeling for $Ca_V1.4$ (**Fig. 1b**). Some abnormalities were apparent in G369i KI cone pedicles, such as extremely elongated ribbons and telodendria extending towards the inner nuclear layer (**Fig.1b**). These results indicate that $Ca_V1.4$ Ca^{2+} signals are dispensable for the integrity of ribbons and the pedicle but are necessary for their overall refinement.

Ca_V3 channel activity is present in cones of G369i KI and $Ca_V1.4$ KO mice but not WT mice, ground squirrel, or macaque retina

A prevailing yet unsupported hypothesis regarding the relatively mild visual phenotypes in CSNB2 is that additional Ca_V subtypes may compensate for $Ca_V1.4$ loss-of-function in cones. If so, then Ca^{2+} currents (I_{Ca}) mediated by these subtypes should be evident in cones of $Ca_V1.4$ KO and G369i KI mice. To test this, we performed patch clamp recordings of cones in retinal slices of adult WT, G369i KI, and $Ca_V1.4$ KO mice under conditions designed to isolate I_{Ca}. During voltage ramps in WT cones, I_{Ca} activated around −50 mV and peaked near −20 mV, consistent with the properties of $Ca_V1.4$ (**Fig. 2a-d**). While not observed in rods of G369i KI or $Ca_V1.4$ KO mice[19], a small-amplitude I_{Ca} that activated around −60 mV and peaked near −35 mV was detected in cones of these mice (**Fig.2a-d**). To uncover this low voltage-activated I_{Ca}, we used a faster voltage ramp (0.5 mV/ms) than in the previous study of G369i KI rods (~0.15 mV/ms)[19]. With this faster voltage ramp, I_{Ca} was not apparent in G369i KI rods (**Supp.Fig.S1**). Therefore, the aberrant I_{Ca} is an adaptation to $Ca_V1.4$ loss-of-function in cones but not rods.

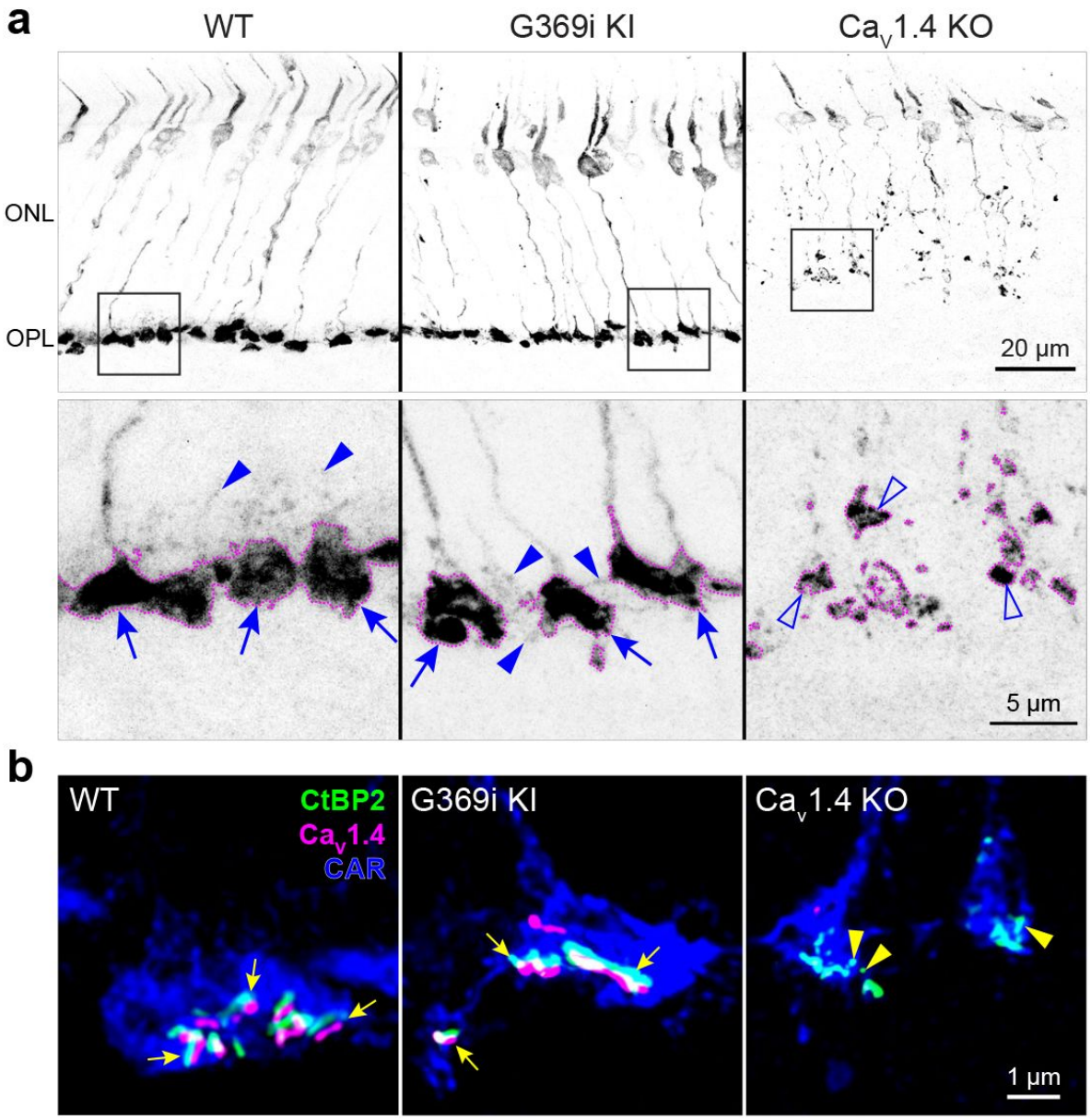

Figure 1.

Cone pedicles and the mutant Ca$_V$1.4 G369i channel are normally localized in the retina of G369i KI mice but not Ca$_V$1.4 KO mice.

Confocal images of the outer nuclear layer (ONL) and outer plexiform layer (OPL) of retina from WT, G369i KI, and Ca$_V$1.4 KO mice that were labeled with antibodies against cone arrestin (CAR), CtBP2, and Ca$_V$1.4. *a*, Inverted images of CAR labeling. Lower panels depict pedicles labeled by CAR antibodies (dotted outlines) and correspond to the boxed regions in the upper panels. Cone pedicles remain in the OPL of WT and G369i KI retina (arrows) but are misshapen and retracted into the ONL of the Ca$_V$1.4 KO retina (open arrowheads). Solid arrowheads indicate telodendria which extend only apically in WT retina but extend basally and laterally in G369i KI retina. *b*, Deconvolved confocal images showing Ca$_V$1.4 labeling near cone ribbons in WT and G369i KI pedicles (arrows) and ribbon spheres without Ca$_V$1.4 labeling in the Ca$_V$1.4 KO pedicle (arrowheads). Rod-associated CtBP2 and Ca$_V$1.4 labeling was removed for clarity.

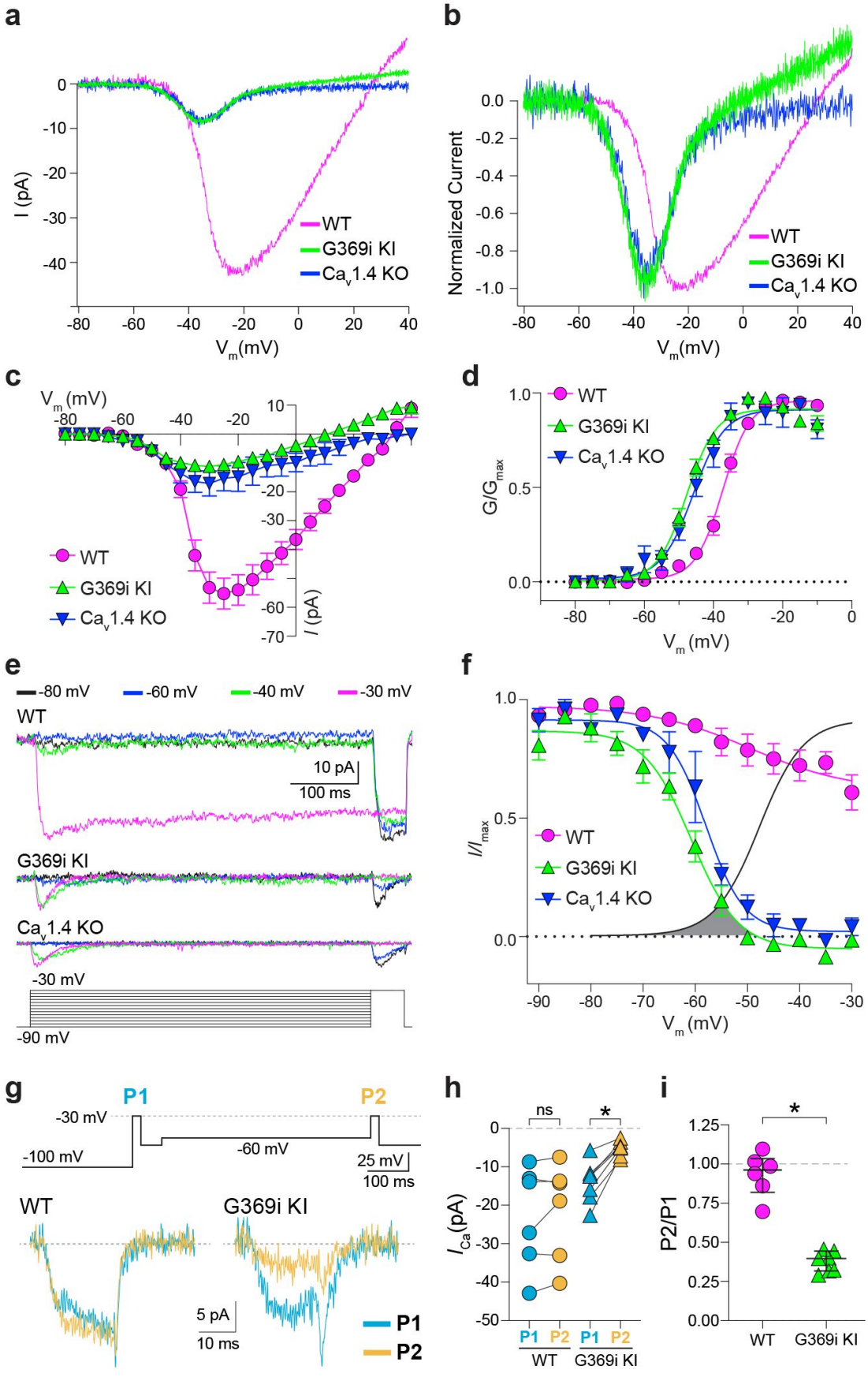
a
I (pA)
V_m(mV)
WT
G369i KI
Ca_v1.4 KO
b
Normalized Current
V_m(mV)
WT
G369i KI
Ca_v1.4 KO
c
V_m (mV)
I (pA)
WT
G369i KI
Ca_v1.4 KO
d
G/G_max
V_m (mV)
WT
G369i KI
Ca_v1.4 KO
e
-80 mV
-60 mV
-40 mV
-30 mV
WT
10 pA
100 ms
G369i KI
Ca_v1.4 KO
-30 mV
-90 mV
f
I/I_max
V_m (mV)
WT
G369i KI
Ca_v1.4 KO
g
P1
P2
-30 mV
-100 mV
-60 mV
25 mV
100 ms
WT
G369i KI
5 pA
10 ms
P1
P2
h
ns
*
I_Ca(pA)
P1 P2 P1 P2
WT
G369i KI
i
*
P2/P1
WT
G369i KI

Figure 2.

A low-voltage activated I_{Ca} is present in cones of G369i KI and $Ca_V1.4$ KO but absent in cones of WT mice.

a, Representative traces of I_{Ca} evoked by voltage ramps. ***b***, I_{Ca} traces from *a* normalized to their peak current amplitude to illustrate the hyperpolarizing shift in the I-V from cones of G369i KI and $Ca_V1.4$ KO mice. ***c,d***, I-V (*c*) and G-V (*d*) relationships for I_{Ca} evoked by 50 ms, +5 mV increments from a holding voltage of −90 mV. V_m, test voltage. WT, n = 13; G369i KI, n = 9; $Ca_V1.4$ KO, n = 3. ***e***, Representative I_{Ca} traces and voltage protocol (bottom) for steady-state inactivation. I_{Ca} was evoked by a conditioning pre-pulse from −90 mV to various voltages for 500 ms followed by a test pulse to −30 mV for 50 ms. ***f***, Steady-state inactivation data from cones as recorded in *e*. I/I_{max} represents the current amplitude of each −30-mV test pulse (I) normalized to current amplitude of the −30-mV test pulse preceded by a −90 mV conditioning pre-pulse (I_{max}) and was plotted against pre-pulse voltage. Shaded region indicates window current for G369i KI cones. Line without symbols represents G-V curve for G369i KI cones replotted from *d*. WT, n = 8; G369i KI, n = 8; $Ca_V1.4$ KO, n = 3. In graphs *c,d,* and *f,* smooth lines represent Boltzmann fits, symbols and bars represent mean ± SEM, respectively. ***g,*** Representative I_{Ca} traces from WT and G369i KI cones and voltage protocol (top). I_{Ca} was evoked by a step from - 100 mV to −30 mV before (P1) or after (P2) a 500 ms step to −60 mV. ***h,i,*** Graphs depicting peak amplitude of I_{Ca} during P1 and P2 steps (*h*) and the ratio of the amplitudes of I_{Ca} evoked by P2 and P1 pulses (P2/P1; *i*) from cones recorded as in *g*. WT, n = 6; G369i KI, n = 6, *p < 0.05 by paired t-test.

We next used step depolarizations to identify the type of Ca_v channel underlying I_{Ca} in G369i KI and $Ca_V1.4$ KO cones. Analysis of current-voltage (I-V) and conductance-voltage (G-V) relationships revealed a significant, hyperpolarizing shift (~10 mV) in the voltage of half maximal activation (V_h) in G369i KI cones (**Fig.2c,d**; **Table 1**). I_{Ca} in G369i KI cones was not sustained as in WT cones but inactivated rapidly during 500-ms step depolarizations (**Fig. 2e**). For G369i KI cones, overlay of the conductance-voltage (**Fig. 2d**) and inactivation curves revealed a sizeable window current (**Fig. 2f**). These features of I_{Ca} in G369i KI and $Ca_V1.4$ KO cones resembled those of Ca_v3 T-type channels rather than $Ca_V1.4$[20].

In a previous study, a Ca_v3-like current was detected in patch clamp recordings of cone pedicles in WT mouse cones[21]. However, in recordings of WT mouse cone somas, we did not observe a low-voltage activated component in the I-V or G-V curves that would be indicative of a Ca_v3 subtype (**Fig.2c,d**). To further test for a Ca_v3 contribution to I_{Ca} in WT mouse cones, we used a double pulse voltage protocol where I_{Ca} was evoked before (P1) and after (P2) a 500-ms step to −60 mV (**Fig.2g**). With this protocol, the inactivation of Ca_v3 channels by the −60 mV step should lead to a reduction in the amplitude of the P2 vs the P1 current. While such a reduction was clearly evident in cones of G369i KI mice (i.e., P2/P1 < 1), there was no significant difference in the P2 and P1 currents in cones of WT mice (**Fig.2g-i**).

We also used antagonists selective for Ca_v1 and Ca_v3 channels (isradipine and ML 218, respectively). As expected, I_{Ca} in WT cones was significantly but incompletely suppressed by isradipine (**Fig. 3a,b**). The V_h of the I-V was similar before (−36.5 ± 0.8 mV) and after (−38.3 ± 1.8 mV) perfusion of isradipine (t(3,4)=0.90, p = 0.43 by paired t-test), suggesting that the residual I_{Ca} after exposure to isradipine arose from unblocked $Ca_V1.4$ rather than Ca_v3 channels. While ML 218 modestly inhibited I_{Ca} in some WT cones, the effect was not statistically significant (**Fig. 3c,d**) and could be attributed to weak activity on $Ca_V1.4$. In transfected HEK293T cells, ML 218 modestly inhibited I_{Ca} and caused a negative shift in the V_h for $Ca_V1.4$, in contrast to its strong inhibition of $Ca_v3.2$ (**Supp.Fig. S2**). Like its effects on $Ca_v3.2$, ML 218 nearly abolished I_{Ca} in cones of G369i KI mice whereas isradipine had little effect (**Fig. 3a-d**).

	C_M (pF)	P-value	n	R_M (MΩ)	P-value	n
WT	4.88 (3.86, 5.01)	--	11	3.57 (2.81, 4.65)	--	11
G369i KI	4.08 (3.88, 4.34)	0.73[a]	9	5.06 (4.04, 8.24)	0.04[a]	9
$Ca_v1.4$ KO	3.31 (3.00, 3.76)	0.001[a], 0.04[b]	6	8.21 (7.26, 9.06)	0.001[a], 0.47[b]	6
G-V	V_h (mV)	P-value	n	*k*	P-value	n
WT	-37.54 (-38.91, -35.13	--	13	2.75 (2.47, 4.32)		13
G369i KI	-47.59 (-50.07, -46.72)	0.0001[a]	9	2.99 (2.68, 4.16)	0.99[a]	9
$Ca_v1.4$ KO	-44.98 (-50.15, -43.27)	0.085[a], 0.99[b]	3	4.33 (3.73, 5.22)	0.34[a], 0.49[b]	3
Steady state inactivation	V_h (mV)	P-value	n	*k*	P-value	n
WT	-49.06 (-57.95, -41.82)	--	8	-7.25 (-12.30, -4.97)	--	8
G369i KI	-59.40 (-62.73, -58.01)	0.01[a]	8	-3.81 (-5.23, -2.46)	0.12[a]	8
$Ca_v1.4$ KO	-56.62 (-61.65, -56.56)	0.88[a], 0.88[b]	3	-3.67 (-5.17, -1.19)	0.14[a], 0.99[b]	3
	Tau activation	P-value	n	Tau deactivation	P-value	n
WT	2.04 (1.26, 2.71)	--	11	0.88 (0.62. 2.09)	--	6
G369i KI	3.32 (2.99, 4.06)	0.001[a]	9	3.40 (2.62, 4.34)	0.004[a]	6

Values represent median (25^{th}, 75^{th} quartiles). V_h and *k* were determined from Boltzmann fits of the G-V and steady-state inactivation curves. Time constant (tau) for activation was obtained from exponential fit of the rising phase of I_{Ca} evoked by a 50-ms test pulse to a voltage near the peak of the I-V. Tau deactivation was determined from exponential fit of the decay of the tail current evoked by repolarization to -90 mV from +20 mV. C_M, membrane capacitance; R_M, input resistance. P-values were determined by Kruskal Wallis test. [a], relative to WT. [b], relative to G369i KI.

Table 1.

Comparison of parameters from electrophysiological recordings of cones.

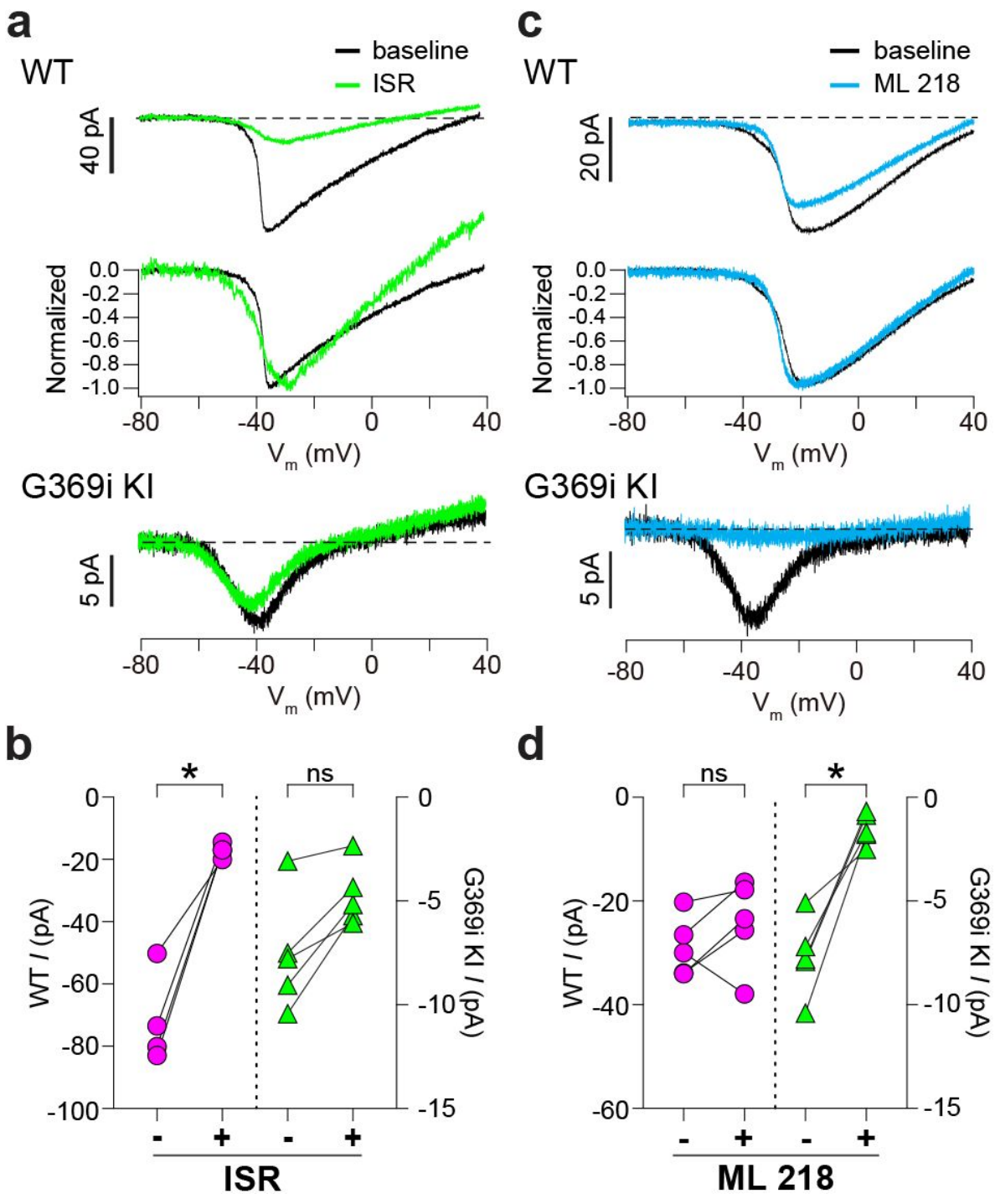

Figure 3.

Pharmacological characterization of I_{Ca} in cones of WT and G369i KI mice.

a, Representative traces for I_{Ca} evoked by voltage ramps in cones of retinas from WT (top) and G369i KI (bottom) mice before (baseline) and after exposure to isradipine (ISR, 1 μM). Middle panel, WT I_{Ca} from voltage ramps in the top panel were normalized to their peak I_{Ca} to clarify the similar properties of I_{Ca} before and after ISR exposure. ***b,*** Peak I_{Ca} before (−) and during (+) ISR exposure from cones as recorded in *a*. WT, n = 4; G369i KI, n = 5; *p < 0.05 by paired t-test. ***c,*** Representative traces for I_{Ca} evoked by voltage ramps in cones of retinas from WT or G369i KI mice before (baseline) and after exposure to ML 218 (5 μM). Middle panel, WT I_{Ca} from voltage ramps in the top panel were normalized to their peak I_{Ca} to clarify the similar properties of I_{Ca} before and after ML 218 exposure. ***d,***
Peak I_{Ca} before (−) and during (+) ML 218 exposure. WT, n = 5; G369i KI, n = 5; *p < 0.05 by paired t-test.

Finally, we recorded from ground squirrel and macaque cones, where the large amplitude of I_{Ca} facilitates pharmacological and biophysical analyses. Consistent with its actions on $Ca_v1.4$ in WT mouse cones (**Fig. 3b**) and transfected HEK293T cells (**Supp.Fig. S2**), ML 218 caused an insignificant inhibition of peak I_{Ca} (−7.0 ± 20.8%, n = 6 cones) as well as a negative shift in the voltage-dependence of activation in ground squirrel cones ($\Delta V_{1/2}$ = −1.16 ± 0.94 mV, n = 6, mean ± SD, p = 0.029, t-test; **Fig. 4a,b**). By contrast, application of isradipine dramatically suppressed I_{Ca} in cones in various regions of the ground squirrel retina (**Fig. 4c,d**). Subsequent application of ML 218 did not reveal a Ca_v3-like current: the I-V and G-V of the isradipine + ML 218-sensitive current were shifted in the positive rather than the negative direction relative to the isradipine-sensitive current (**Fig.4c-g**). This result is consistent with the time- and voltage-dependent block of Ca_v1 channels by dihydropyridine antagonists such as isradipine [22]. As a positive control, we confirmed that ML 218 blocked a prominent Ca_v3-type current in ground squirrel type 3a OFF cone bipolar cells (**Fig.4h,i**). In recordings of macaque cone pedicles, we compared the properties of I_{Ca} using a holding voltage of −90 mV or −50 mV, the latter of which should inactivate Ca_v3 channels (**Fig.5a**). There was no difference in the I-V or G-V relationships obtained at these holding voltages (**Fig.5b-e**). As in WT mouse cones (**Fig.2g-i**), there was also no difference in I_{Ca} recorded before and after an inactivating pulse to −60 mV (**Fig.5f,g**). We conclude that Ca_v3 channels do not normally contribute to I_{Ca} in cones of WT mice, ground squirrel, and macaque.

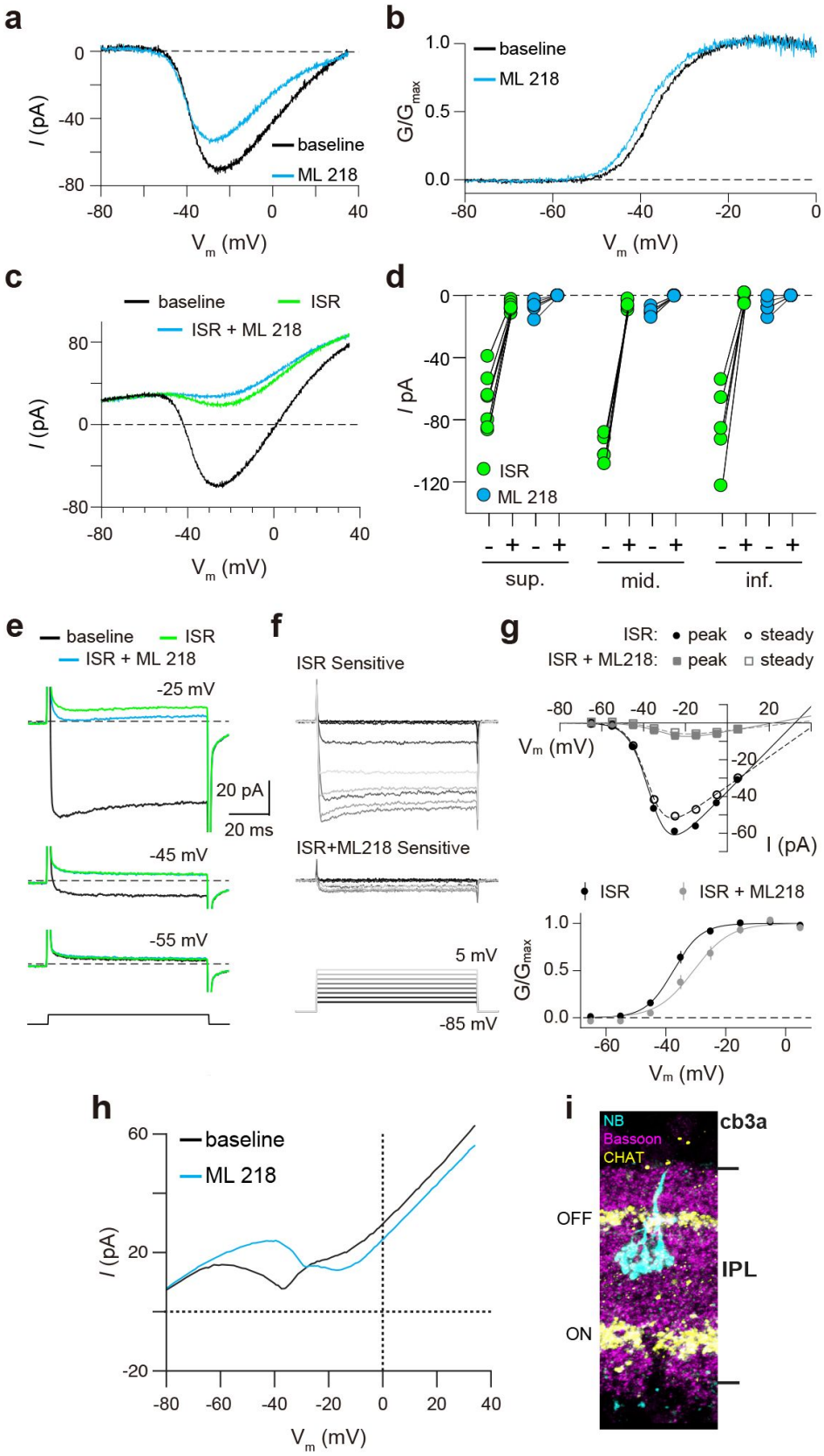
a
I (pA)
baseline
ML 218
V_m (mV)
b
G/G_max
baseline
ML 218
V_m (mV)
c
baseline
ISR
ISR + ML 218
I (pA)
V_m (mV)
d
I pA
ISR
ML 218
sup.
mid.
inf.
e
baseline
ISR
ISR + ML 218
-25 mV
20 pA
20 ms
-45 mV
-55 mV
f
ISR Sensitive
ISR+ML218 Sensitive
5 mV
-85 mV
g
ISR: peak steady
ISR + ML218: peak steady
V_m (mV)
I (pA)
ISR
ISR + ML218
G/G_max
V_m (mV)
h
baseline
ML 218
I (pA)
V_m (mV)
i
NB
Bassoon
CHAT
cb3a
OFF
IPL
ON

Figure 4.

Pharmacological characterization of I_{Ca} in ground squirrel cones.

a, Representative traces corresponding to baseline-corrected I_{Ca} evoked by voltage ramps before (baseline) and during application of ML 218. ***b,*** G-V relationship of I_{Ca} in *a*. ***c,*** Representative traces corresponding to I_{Ca} evoked by voltage ramps in control (baseline) and in ISR (2 μM) alone or in ISR+ML 218 (5 μM). ***d,*** Peak I_{Ca} from cones including the record from *c* before (−) and during (+) ISR or ISR+ML 218 block. The changes during the addition of ML218 were small but significant (sup., n = 7, ISR: p < 0.0001, ML218: p = 0.0047; mid., n = 5, ISR: p < 0.0001, ML218: p = 0.0001; inf., n = 5, ISR: p = 0.0019, ML218: p = 0.0460; two-tailed t test) and were likely due to a further non-specific, time-dependent reduction in the Ca_V1 current. ***e,*** I_{Ca} was evoked by steps from −85 mV to voltages between −65 and −5 mV in increments of +10 mV (protocol shown below the current traces in *f*). Representative traces are shown in control, ISR, or ISR+ML 218. Current traces during steps to −55 and −45 mV lacked both transient and ML 218-senstive components. Dashed lines indicate zero current. ***f,*** Traces show the I_{Ca} sensitive to ISR (top) and ISR+ML218 (middle). The I_{Ca} recorded in ISR was subtracted from the baseline I_{Ca} (top). I_{Ca} recorded in ISR+ML218 was subtracted from I_{Ca} recorded in ISR (middle). ***g,*** *Top*, I-V relationship of peak and steady-state I_{Ca} from *f*. *Bottom*, G-V relationship of the I_{Ca} blocked by ISR and ISR + ML218. Smooth lines represent Boltzmann fits. Symbols and bars represent mean ± SEM (n = 4 cones). Due a negative shift in the activation properties caused by ML 218 on a residual Ca_V1 current that is assumed to remain at the end of the experiment, the G-V curve of the I_{Ca} isolated through subtraction by applying ISR+ML 281 underwent a statistically insignificant shift to the right. Data presented in *e-g* are from the same cone. ***h,*** Representative I_{Ca} traces from voltage ramps in an OFF cb3a bipolar cell before and during the application of ML 218. $V_{1/2}$ was shifted to the right by 13.1 ± 4.3 mV (n = 3 cb3a cells, mean ± SD) consistent with the block of a Ca_V3-like conductance. In cb3b OFF bipolar cells, ML 218 produced only a slight leftward shift in an I_{Ca} that had a more depolarized activation range, consistent with the exclusive expression a Ca_V1-type current ($\Delta V_{1/2}$ = −1.9 ± 0.4 mV, n = 3 cells; data not shown). ***i,*** Neurobiotin fill shows cb3a axon stratification and morphology in retina labeled with antibodies against bassoon and choline acetyltransferase (CHAT) to label the OFF and ON sublamina of the IPL.

To test whether the appearance of the Ca_V3-mediated I_{Ca} in G369i KI cones could result from an increase in the expression of a specific Ca_V3 subtype (*i.e.*, $Ca_V3.1$, $Ca_V3.2$, or $Ca_V3.3$), we initially tried labeling with commercially available antibodies against $Ca_V3.2$. However, the data were unreliable since these antibodies produced a similar labeling pattern in $Ca_V3.2$ KO retinal tissue (data not shown). As an alternative, we performed single cell RNA sequencing on cells isolated from the retina of WT and G369i KI mice (**Supp. Fig.S3**). We sequenced 28,782 cells and, with unsupervised clustering at resolution=0.5, we grouped the cells into 20 clusters. Clusters 8 and 16 were identified as cones based on the expression of cone marker genes (e.g., Opn1sw, Opn1mw, Arr3, Gnat2). Consistent with previous studies[21], [23], *Cacna1h* encoding the $Ca_V3.2$ subtype was the major Ca_V3 transcript expressed in WT mouse cones. There was no significant difference in *Cacna1h* expression between WT and G369i KI cones according to this analysis (**Supp. Fig.S3**). Thus, the enhanced activity of Ca_V3 channels in cones of G369i KI mice results from a mechanism other than increased transcription of *Cacna1h*.

Cone synapses are enlarged with some errors in postsynaptic wiring in G369i KI mice

The replacement of $Ca_V1.4$ with Ca_V3 as the primary conduit for Ca^{2+} influx in G369i KI cones allowed us to dissect the importance of $Ca_V1.4$ Ca^{2+} signals for the molecular and structural organization of the cone synapse. To this end, we first analyzed WT and G369i KI cone synapses by immunofluorescence and confocal microscopy. Presynaptic proteins such as bassoon and members of the postsynaptic signaling complex in depolarizing (ON) cone bipolar cells (GPR179, mGluR6, and TRPM1[24]) were enriched near cone ribbons in G369i KI mice as in WT mice (**Fig. 6a**). Compared to WT mice, the labeled structures in G369i KI mice occupied a larger volume

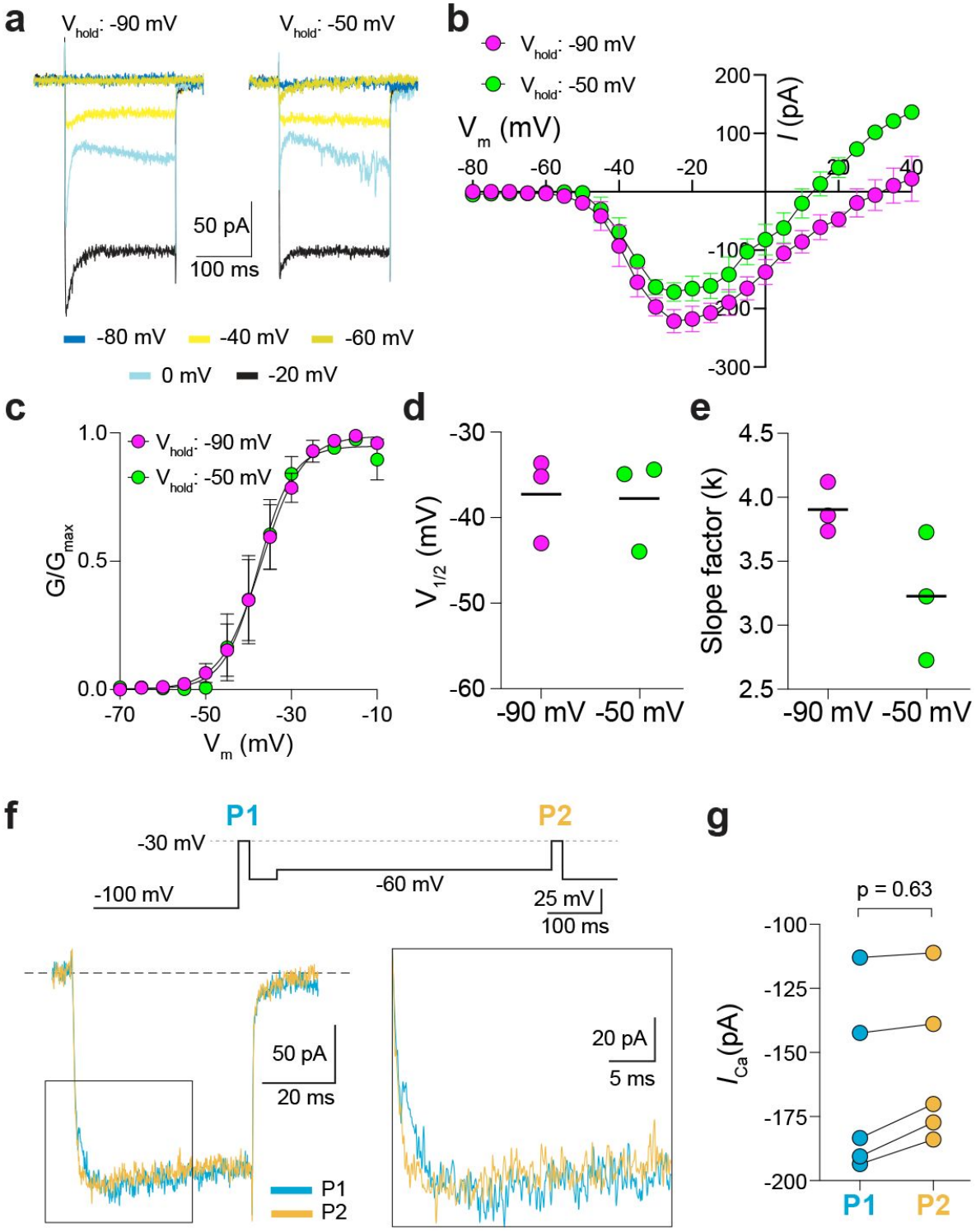

Figure 5.

Characterization of I_{Ca} in patch clamp recordings of cone pedicles of macaque retina.

a-c, Representative current traces (*a*) and corresponding I-V (*b*) and G-V (*c*) relationships for I_{Ca} evoked by 200-ms steps from a holding voltage of −90 mV or −50 mV. n = 3 cones. ***d,e,*** $V_{1/2}$ (*d*) and slope factor (*e*) obtained from Boltzmann fit of data in *c*. p = 0.50 in *d*; p = 0.25 in *e* by Wilcoxon matched pairs signed rank test. ***f,*** Voltage protocol (*top*) and representative I_{Ca} traces (*bottom left*) from cones as recorded in **Fig. 2g-i**. Bottom right, expanded view of the boxed region in the left traces. ***g,*** Peak I_{Ca} during P1 and P2 steps from cones recorded as in *f*. n = 5 cones, p = 0.62 by Wilcoxon matched pairs signed rank test.

(**Fig. 6b,c**) but were of lower intensity (**Fig. 6d**), suggesting an increase in the spread rather than in the levels of synaptic proteins. Unlike in WT mice, the volume of presynaptic and postsynaptic proteins increased linearly with the volume of the pedicle in G369i KI mice (**Fig. 6e-i**). These results show that the molecular determinants of the cone synapse can assemble in G369i KI mice but change in their sub-synaptic distribution in ways that correlate with the expansion of the cone pedicle.

The cone synapse is structurally complex, with the dendritic tips of two horizontal cells and an intervening ON cone bipolar cell invaginating deeply into the pedicle near the ribbon [3]. To test how the switch in Ca_V subtypes might affect this arrangement of postsynaptic partners, we generated 3D reconstructions of cone synapses by serial block-face scanning electron microscopy (SBFSEM; **Fig. 7**). As with the enlarged synaptic contacts (**Fig. 6**), structural modifications in G369i KI pedicles were evident. Compared to WT, ribbons in G369i KI pedicles appeared disorganized and were often parallel rather than perpendicular to the presynaptic membrane (**Fig.7a-c**). Consistent with our confocal analyses (**Fig.1**), G369i KI cone pedicles extended telodendria in multiple directions rather than just apically (**Fig. 7a**). In addition, a slightly larger fraction of synaptic sites in the G369i KI pedicle (35% vs 14% in WT) formed incorrect postsynaptic partnerships including with glia (**Fig.7b-d**'; **Table 2**). Nevertheless, the number of ribbons is normal in G369i KI cones and about half of the ribbons make invaginating contacts with the appropriate cell types (*i.e.*, both horizontal cells and cone bipolar cells; **Table 2**). On average, there were more vesicles associated with ribbons in cones of G369i KI mice (245 per ribbon) than of WT mice (178 per ribbon; **Table 2**), but the difference did not reach statistical significance. Together with our immunofluorescence data, these results indicate that cone synapses undergo relatively subtle morphological changes in G369i KI mice, perhaps in response to the loss of $Ca_V1.4$ Ca^{2+} signals.

Postsynaptic responses to light are present in horizontal cells of G369i KI mice but not $Ca_V1.4$ KO mice

Compared to $Ca_V1.4$ KO mice, the relative preservation of cone synapses in G369i KI mice allowed the unique opportunity to test whether a Ca_V subtype other than $Ca_V1.4$ could support synaptic release. To this end, we analyzed synaptic transmission between cones and horizontal cells (HCs). In darkness, glutamate released from cones depolarizes horizontal cells via activation of α-amino-3-hydroxy-5-methyl-4-isoxazolepropionic (AMPA)/kainate receptors[25, 26]. The resulting excitatory postsynaptic current (EPSC) undergoes a decline in response to light stimuli that hyperpolarize cones[27]. In WT HCs, a 1-s light flash (λ=410 nm) inhibited the standing EPSC, which is reflected as an outward (hyperpolarizing "ON") current (**Fig. 8a**). Upon termination of the light, an inward (depolarizing "OFF") current signaled the resumption of the EPSC (**Fig. 8a**). Both the ON and OFF responses in WT HCs increased with light intensity, reflecting the impact of luminance on the presynaptic membrane potential of cones and the subsequent change in glutamate release from their terminals (**Fig. 8b**).

Consistent with the lack of mature ribbons and abnormal cone pedicles (**Fig.1**), HC light responses were negligible in $Ca_V1.4$ KO mice (**Fig.8a,b**). In contrast, the ON and OFF responses were present in G369i KI HCs although significantly lower in amplitude than in WT HCs (**Fig. 8a,b**). As expected, the EPSC in darkness and the light responses were abolished by the AMPA/kainate receptor antagonist, DNQX, in both WT and G369i KI HCs (**Fig. 8c,d**). In addition to its smaller amplitude, the transient nature of the ON response in G369i KI HCs suggested inadequate cessation of cone glutamate release by light (**Fig.8b**). Slow deactivation of Ca_V3 channels and/or their activation at negative voltages[20] could give rise to Ca^{2+} signals that support release following light-induced hyperpolarization of G369i KI cones.

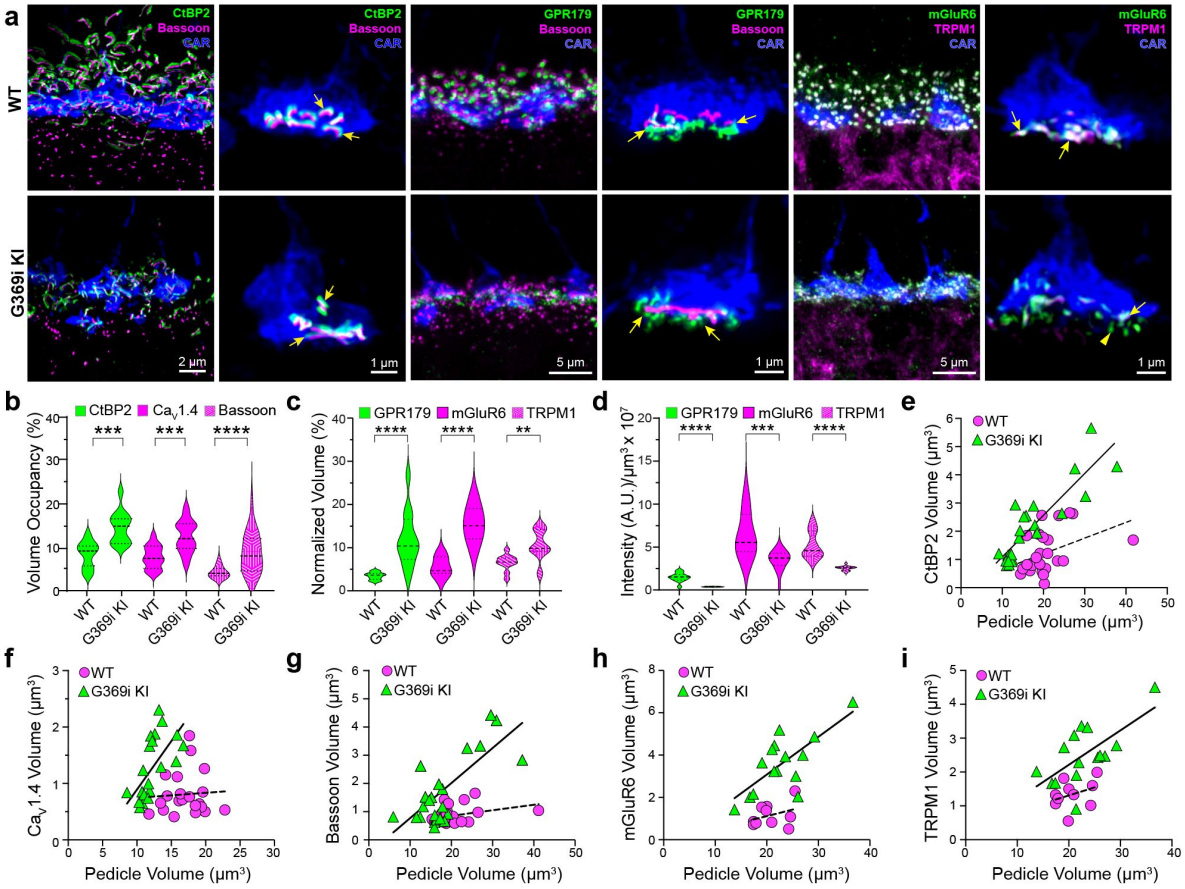

Figure 6.

Immunofluorescence characterization of cone synapses in WT and G369i KI mice.

a, Confocal images of the OPL of WT and G369i KI mice labeled with antibodies against cone arrestin (CAR) and proteins that are presynaptic (CtBP2, bassoon) or postsynaptic (GPR179, TRPM1, mGluR6). Every other panel shows high-magnification, deconvolved images of single pedicles labeled with cone arrestin (rod spherule-associated signals were removed for clarity). Arrows indicate ribbon synapses, which appear enlarged in the G369i KI pedicles. ***b***, Violin plot representing volume of presynaptic protein labeling normalized to the volume of their respective CAR-labeled pedicles (volume occupancy). ***c,*** Violin plot representing volume of postsynaptic protein labeling normalized to the volume of their respective CAR-labeled pedicles. ***d,*** Violin plot representing fluorescence intensity of postsynaptic proteins. For *b-d*, **p < 0.01, ***p < 0.001, ****p < 0.0001, unpaired t-tests. ***e-i***, Dependence of synapse size on pedicle size. Volumes corresponding to labeling of CtBP2 (*e*: p = 0.051, r = 0.4 for WT; p < 0.0001, r = 0.88 for G369i KI), $Ca_V1.4$ (*f*: p = 0.8, r = 0.06 for WT; p = 0.002, r = 0.88 for G369i KI), bassoon (*g*: p = 0.1, r = 0.34 for WT; p < 0.0001, r = 0.75 for G369i KI), mGluR6 (*h*: p = 0.32, r = 0.35 for WT; p = 0.002, r = 0.73 for G369i KI) and TRPM1 (*i*: p = 0.32, r = 0.35 for WT; p = 0.007, r = 0.66 for G369i KI) are plotted against pedicle volume. Dashed and solid lines represent fits by linear regression for WT and G369i KI, respectively.

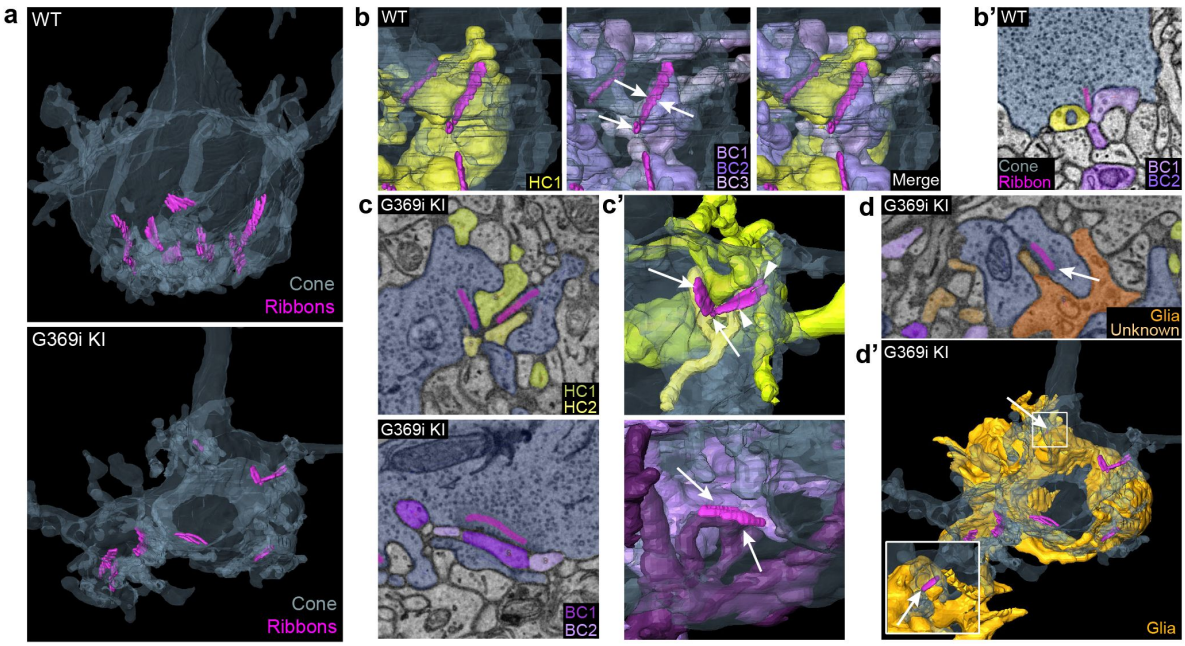

Figure 7.

Three-dimensional reconstruction of cone synapses by SBFSEM.

Reconstructions were made of WT and G369i KI pedicles (n = 2 each). ***a***, 3D renderings showing ribbons (magenta) within cone pedicles (gray) from WT and G369i KI mice. ***b,*** 3D renderings show ribbon sites in a WT cone pedicle contacting one horizontal (HC1; yellow) and three bipolar cells (BC1-3; purple). ***b',*** Raw image from *b* shows a single plane example of BC1-2 and HC1 contacting the ribbon site. ***c-d',*** Single plane raw (*c,d*) images and 3D reconstructions (*c',d'*) show ribbon sites within the G369i KI cone pedicle contacting in *c,c'*: horizontal cells (HC1-2) only (upper panels), CBCs (BC1-2) only (lower panels); and in *d,d'*: a glial cell (orange) and an unknown partner. The glial cell completely envelops the pedicle. Inset in *d'* shows glial-contacting ribbon site (arrow). In other panels, arrows indicate points of contact between ribbons and other postsynaptic elements.

	WT		G369i KI	
	Cone 1	Cone 2	Cone 1	Cone 2
# of ribbons	12	8	8	6
Mean # synaptic vesicles per ribbon	137.75	218.25	224	267.5
Type of contact: % total (fraction of total)				
Invaginating	58.3 (7/12)	87.5 (7/8)	50 (4/8)	50 (3/6)
Non-invaginating	41.7 (5/12)	12.5 (1/8)	50 (4/8)	50 (3/6)
Partner composition: % total (fraction of total)				
HC/BC	83.3	87.5	50.0	66.7
HC only	8.3	12.5	25.0	33.3
BC only	8.3	0	12.5	0
Glia only	0	0	12.5	0

Results represent analysis of n = 2 pedicles reconstructed by serial block face scanning electron microscopy in images obtained from WT or G369i KI mice (N= 1 animal each). The first row of vesicles encircling and immediately apposed to the ribbon were quantified for all the z-planes of the ribbon. Sites were counted as 'invaginating' if postsynaptic partners were enveloped on all sides by the cone terminal for at least a couple of consecutive image planes.

Table 2.

Comparison of parameters for cone synapse organization

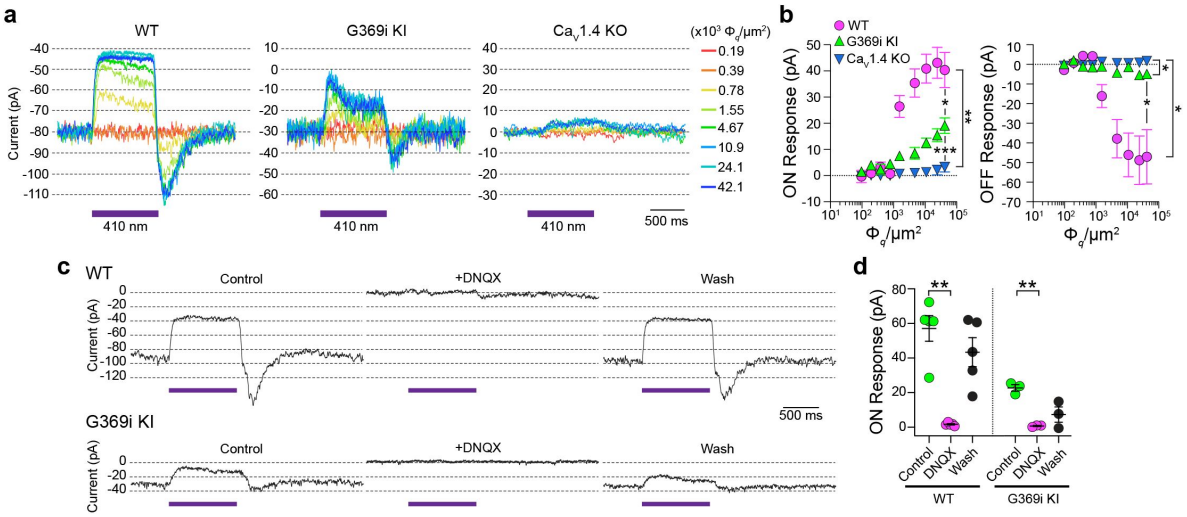

Figure 8.

Patch clamp recordings of light responses of horizontal cells in WT, G369i KI and $Ca_V1.4$ KO mice.

a-b, Representative traces from whole-cell patch clamp recordings of horizontal cells held at −70 mV (*a*) and quantified data (*b*) for currents evoked by 1 s light flashes (λ = 410 nm) plotted against light intensities. In *b*, peak current amplitudes during (ON Response) and after (OFF Response) the light stimuli were plotted against photon flux per µm^2 (Φ_q/µm^2). Data represent mean ± SEM. WT, n = 8; G369i KI, n = 13; $Ca_V1.4$ KO, n = 8. There was a significant difference in responses of WT, G369i KI, and $Ca_V1.4$ KO horizontal cells. For ON responses, $F(16, 216) = 22$, $p < 0.0001$ by two-way repeated measures ANOVA, Tukey's multiple comparisons post-hoc test. For OFF responses, $F(16, 216) = 13.61$, $p < 0.0001$ by two-way repeated measures ANOVA, Tukey's multiple comparisons post-hoc test. ***c-d,*** Representative traces from horizontal cells held at −70 mV (*c*) and quantified data (*d*) for currents evoked by 1-s light flashes (λ= 410 nm, 1.2 x 10^5 Φ_q/µm^2) before, during, and after washout of DNQX (20 µM). In *d,* symbols represent responses from individual cells, n = 5 cells for WT and 3 cells for G369i KI, bars represent mean ± SEM. **, $p < 0.01$ by paired t-tests.

To test if the diminished HC light responses correlated with lower presynaptic Ca^{2+} signals in G369i KI cones, we performed 2-photon imaging of cone pedicles filled with the Ca^{2+} indicator Fluo3 and labeled with Alexa-568-conjugated peanut agglutinin. In WT cones, depolarization by K^+ (50 mM) caused a sustained increase of Ca^{2+} ($\Delta F/F_0$ = 1.85 ± 0.1, n = 11 terminals) that was significantly lower after the addition of isradipine ($\Delta F/F_0$ = 1.44 ± 0.07, p = 0.0015 by repeated measures one-way ANOVA with Tukey's multiple comparison posthoc test; F[1.608, 16.08] = 55.17; p < 0.0001; **Fig.9a,b**). The Ca^{2+} signal remaining in the presence of isradipine could arise from unblocked $Ca_V1.4$ channels and/or Ca^{2+} release from intracellular stores[28]. In G369i KI cones, the peak amplitude of the K^+-evoked Ca^{2+} signal ($\Delta F/F_0$ = 1.07 ± 0.02, n = 14 terminals) was significantly lower than in WT cones (t(23)=8.74, p < 0.0001 by unpaired t-test, n = 14 terminals). The decrease in the Ca^{2+} signal in the G369i KI cone pedicles during isradipine exposure paralleled that during the depolarization (**Fig.9a**), suggesting it was not a consequence of Ca_V1 blockade. The lower amplitude and more transient Ca^{2+} signals mediated by Ca_V3 channels may be cleared more rapidly in G369i KI cones as compared to prolonged $Ca_V1.4$-initiated Ca^{2+} signals in WT cones. Taken together, our results suggest that Ca_V3 channels nominally support Ca^{2+} signals and synaptic transmission in cones of G369i KI mice.

Light responses of bipolar cells and visual behavior are present in G369i KI but not $Ca_V1.4$ KO mice

While HCs play important roles in lateral inhibition of photoreceptor output, the vertical dissemination of visual information from cones to the inner retina is relayed by glutamate to ON and OFF cone bipolar cells (CBCs) which express mGluR6 and AMPA/kainate receptors, respectively. To test for the existence of cone to CBC transmission in G369i KI mice, we recorded electroretinograms (ERGs) under light-adapted conditions using $Ca_V1.4$ KO mice as a negative control (**Fig. 10a-d**). In these recordings, the light-induced response of photoreceptors and the postsynaptic response of ON CBCs corresponds to the a- and b-waves, respectively. Unlike in $Ca_V1.4$ KO mice, the a-waves of G369i KI mice resembled those in WT mice, which indicates that cones do not degenerate in this mouse strain (**Fig. 10a,b**). While greatly reduced in amplitude, the b-wave was measurable in G369i KI mice and significantly larger than in $Ca_V1.4$ KO mice at the highest light intensities (F(14,104)=41, p<0.0001, post-hoc Tukey's p=0.0038 at 2.3 log cd·s/m^2; **Fig. 10a,b**). We also recorded flicker ERGs using 10 Hz light stimuli that can isolate cone pathways involving both ON and OFF CBCs[29, 30]. In WT mice, flicker responses exhibited two peaks, one at a lower irradiance (−2 log cd·s/m^2) and one at higher irradiance (0.5 log cd·s/m^2; **Fig.10c,d**). The peak at the lower irradiance is attributed to responses in both rod and cone pathways, and the peak at higher irradiance is attributed to responses exclusively in cone pathways[29, 30]. Flicker responses in G369i KI mice showed a similar non-monotonic relation as in WT mice but were significantly lower in amplitude (F(26,143)=51.18, p<0.0001, post-hoc Tukey's p=0.0237 at 2.5 log cd·s/m^2; **Fig.10c,d**). The inverted flicker responses at higher illuminations in G369i KI mice were absent in $Ca_V1.4$ KO mice and may result from the hyperpolarizing contribution of cone-to-OFF CBC transmission (**Fig.10c**).

To test whether the cone synaptic responses in G369i KI mice enable vision-guided behavior, we used a swim test that assesses the ability of mice to identify a visible platform[31]. Under scotopic (dark) conditions, G369i KI and $Ca_V1.4$ KO mice took significantly longer to find the platform compared to WT mice (**Fig. 10e,f**). These results are consistent with flicker response assays (**Fig.10c,d**) as well as the absence of I_{Ca} in rods and rod-to-rod bipolar cell synaptic transmission in G369i KI mice[19]. Under photopic (light) conditions, G369i KI mice but not $Ca_V1.4$ KO mice performed as well as WT mice (**Fig. 10e,f**). Thus, G369i KI mice have enough visual function under photopic conditions to quickly find the platform. Collectively, our results suggest that Ca_V3 channels can support cone synaptic responses that are sufficient for visual behavior in G369i KI but not $Ca_V1.4$ KO mice.

Discussion

The nervous system has remarkable abilities to adapt to pathological perturbations in neuronal activity. In the retina, ablation or degeneration of photoreceptors triggers various postsynaptic mechanisms that maintain some level of visual function in rod or cone pathways. These include remodeling of bipolar cell dendrites and their synapses[32–34] as well as changes in the sensitivity of bipolar cells to photoreceptor input and inhibitory modulation[34, 35]. To our knowledge, this study provides the first evidence for a presynaptic form of homeostatic plasticity that originates within photoreceptors. Using $Ca_V1.4$ KO and G369i KI mice, we identify the upregulation of a Ca_V3 conductance as a common response to $Ca_V1.4$ loss-of-function in cones. However, Ca_V3 channels can only compensate for $Ca_V1.4$ loss-of-function if the basic aspects of cone synapse structure are maintained through expression of the G369i mutant channel. Thus, our results also highlight a crucial, non-conducting role for the $Ca_V1.4$ protein that allows cone synapses to function in the absence of $Ca_V1.4$ Ca^{2+} signals.

A non-canonical role for $Ca_V1.4$ in regulating cone synapse assembly

As shown for rod synapses[19], ribbons and other components of the pre- and post-synaptic complex assemble at cone synapses in G369i KI mice (**Figs. 1**,**6**,**7**). Ca_V3 Ca^{2+} signals are dispensable for this process since their presence in $Ca_V1.4$ KO cones is not accompanied by any semblance of ribbon synapses (**Fig.1b**). An intimate relationship between $Ca_V1.4$ and ribbons is supported by the colocalization of $Ca_V1.4$ and puncta resembling ribbon precursor spheres in the developing OPL[7]. $Ca_V1.4$ interacts directly or indirectly with a variety of ribbon synapse associated proteins including RIM [36], CAST/ERC2 [37], bassoon[38], unc119[39–41], and a major component of the ribbon, RIBEYE[42]. $Ca_V1.4$ could pioneer sites of ribbon assembly perhaps by serving as a docking or nucleation site for the active zone. At the same time, ribbon-associated proteins help cluster $Ca_V1.4$ near ribbons since knockout of these proteins in mice leads to fewer presynaptic $Ca_V1.4$ channels and in some cases shortened ribbons[43]. Regardless of the mechanism, our findings show that the formation of photoreceptor synaptic complexes does not require Ca^{2+} influx through $Ca_V1.4$ channels.

Functional Ca_V3 channels are present in cones in the absence of $Ca_V1.4$ Ca^{2+} signals

Our drop-seq analysis aligns with previous studies indicating that *Cacna1h* is expressed at extremely low levels compared to *Cacna1f* in WT mouse cones (**Supp.Fig.S3**)[23, 44]. However, in contrast to recordings of WT mouse cone pedicles in a previous study[21], we found no evidence for Ca_V3-mediated currents in somatic recordings of cones in WT mice (**Figs.2**,**3**). We do not feel the discrepancy results from the different recording configurations given the electrically compact nature of cones. Moreover, recordings from macaque cone pedicles and from the ellipsoids of cylindrically-shaped ground squirrel cones also did not reveal a Ca_V3-mediated current (**Figs.4**,**5**). We acknowledge that there are caveats of the pharmacological approach used in our study as well as the previous work[21]. For example, dihydropyridine antagonists such as isradipine have relatively low affinity for some Ca_V1 subtypes, including $Ca_V1.4$[22, 45] and have strongly voltage-dependent blocking properties. At a holding voltage of −90 mV, isradipine at 1 μM causes only ~80% inhibition of $Ca_V1.4$ with greater block at depolarized voltages[22], which agrees with our recordings of cones in WT mice (**Fig.3a**) and ground squirrels (**Fig.4b-e**). Moreover, in the low micromolar range, Ca_V3 blockers such as Z944 [46] and ML 218 (**Supp.Fig. S2**) have nonspecific effects on Ca_V1 current amplitude and activation

voltage. Thus, Ca_v channels mediating a I_{Ca} that is suppressed by Ca_v3 blockers and spared by dihydropyridines at negative voltages may be mistakenly categorized as Ca_v3 subtypes. In our experiments, the biophysical properties of the isradipine-sensitive I_{Ca} in cones of WT mice and ground squirrels resembled only those of Ca_v1, whereas those of the ML 218-sensitive I_{Ca} in cones of G369i KI mice resembled only those of Ca_v3. Therefore, we favor the interpretation that Ca_v3 contributes to I_{Ca} in mouse cones only upon silencing of $Ca_v1.4$ either by KO of the corresponding protein or by silencing its conductance.

Since *Cacna1h* expression was similar in WT and G369i KI cones (**Supp.Fig.S3**), what causes the increased Ca_v3 channel activity in the latter? Among the Ca_v3 subtypes, $Ca_v3.2$ is uniquely sensitive to post-translational modifications that facilitate the opening of the channel and/or its cell surface trafficking[47]. For example, $Ca_v3.2$ interacts with the deubiquitinating enzyme USP5 which enhances levels of $Ca_v3.2$ protein levels by suppressing its proteasomal degradation[48]. In addition, $Ca_v3.2$ is phosphorylated by calmodulin-dependent kinase II[49] and cyclin-dependent kinase 5[50], which enhances channel activation and current density, respectively. Further interrogation of our drop-seq dataset could illuminate novel $Ca_v3.2$-regulatory pathways that are modified in G369i KI cones.

Consequences of $Ca_v1.4$ loss of function and relevance for CSNB2

Despite having the same complement of proteins as in WT mice, cone synapses in G369i KI mice were enlarged and made errors in postsynaptic partner selection (**Figs.6**,**7**). While I-V curves indicate similar peak I_{Ca} amplitudes in cones of WT and G369i KI mice near the membrane potential of cones in darkness (−45 to −50 mV[51], **Fig.2a,c**), the strong inactivation of Ca_v3 channels and/or reduced Ca^{2+} release from intracellular stores likely account for the greatly diminished Ca^{2+} signals in G369i KI pedicles (**Fig.9**). Paradoxically, reductions in presynaptic Ca^{2+} in rod photoreceptors correlated with illumination-dependent shrinkage of ribbons *in vivo* and *in vitro*[2, 52, 53]. However, ribbon synapse size increases with low presynaptic Ca^{2+} in zebrafish sensory hair cells[54]. The mechanism involves decreased mitochondrial Ca^{2+} uptake and increase in the redox state of nicotinamide adenine dinucleotide (NAD^+/NADH ratio) [55]. Ca_v3 Ca^{2+} signals may decay too quickly in G369i KI cones (**Fig.9**) to enable mitochondrial Ca^{2+} uptake or other mechanisms that trim ribbons.

An intriguing result was the linear increase in ribbon synapse size with pedicle volume in G369i KI but not in WT mice (**Fig. 6e-i**), which could represent a form of homeostatic synaptic scaling as has been demonstrated at the neuromuscular junction[56, 57]. Similarly, the presence of some non-invaginating contacts with incorrect partner pairings in G369i KI mice (**Fig.7**, **Table 2**) could be an attempt to increase synaptic connectivity to compensate for weakened synaptic output. Consistent with this possibility, diminished presynaptic Ca^{2+} signals and non-invaginating cone synapses also characterize the retina of mice lacking the extracellular $\alpha_2\delta$−4 subunit of $Ca_v1.4$[58]. The cone synapses of G369i KI mice and $\alpha_2\delta$−4 KO mice are clearly functional given that photopic visual behavior is preserved in both mouse strains (**Fig.10e,f**)[58] and, in the case of G369i KI mice, HCs exhibit EPSCs whose amplitude decreases with light and AMPA/kainate receptor blockade (**Fig.8**). Defects in cone synaptic transmission that correlate with aberrant cone synapse morphology and connectivity also typify a mouse strain with a gain-of function mutation in $Ca_v1.4$ linked to CSNB2[59, 60]. Thus, balanced presynaptic Ca^{2+} signals may be needed to encode the correct post-synaptic wiring and structure of the cone synapse.

In addition to structural abnormalities in cone synapses, the inability of Ca_v3 channels to support sustained presynaptic Ca^{2+} entry likely contributed to the impaired light responses in HCs and CBCs in G369i KI mice (**Figs.8**,**10**). Due to their slow activation and strong inactivation [61], Ca_v3 channels are not expected to fuel the Ca^{2+} nanodomains that support fast and sustained components of release, both of which occur only at ribbon sites in cones[1, 62]. Ca_v3 channels may also be located further from the ribbon than $Ca_v1.4$, thus lowering the efficiency of coupling

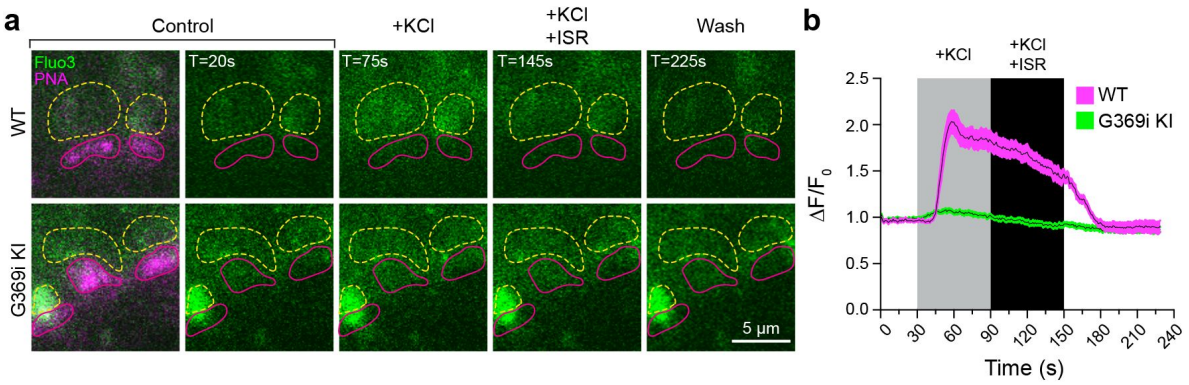

Figure 9.

Ca^{2+} imaging of cone terminals in WT and G369i KI mice.

Depolarization-evoked fluorescence changes (ΔF) were measured by two-photon imaging of Fluo3-filled cone pedicles labeled with PNA-Alexa 568.

a, Representative images at the indicated timepoints (T) before (control), during, and after (wash) bath application of KCl (50 mM) and KCl+ISR (10 μM). For clarity, PNA-Alexa 568 labeling was outlined (magenta, solid circles) and the actual labeling only shown in the initial panel of images. Dashed, yellow circles represent ROIs for analyses. ***b,*** Changes in cone pedicle Fluo3 fluorescence were normalized to the initial fluorescence intensity at time= 0 (ΔF/F0). Solid lines and shaded areas represent the mean ± SEM, respectively. WT, n = 11 pedicles; G369i KI, n = 14 pedicles.

to exocytosis. Regardless of the features that differentiate the contributions of Ca_V3 and $Ca_V1.4$ to cone synaptic release, our findings provide further support for the widely held view that Ca_V1 channels are well-suited to support transmission at ribbon-type synapses.

Based on extremely heterogeneous clinical presentations, CSNB2 manifests as a spectrum of visual disorders that originate from various mutations in *CACNA1F* [14, 63]. Even though some CSNB2 mutant $Ca_V1.4$ channels may traffic normally to the plasma membrane, many of these mutations are expected to produce non-functional, non-conducting $Ca_V1.4$ channels[64, 65]. Yet, the visual phenotypes of CSNB2 patients are not as severe as the complete blindness in $Ca_V1.4$ KO mice, which lack any $Ca_V1.4$ protein expression and exhibit no signs of visual behavior (**Fig.10e,f**)[58]. Collectively, our results suggest that G369i KI mice accurately model $Ca_V1.4$ channelopathies in CSNB2 patients that are characterized by a greater impairment in rod than in cone pathways. This interpretation is supported by our findings that G369i KI mice exhibit horizontal cell responses to bright but not dim illumination (**Fig. 8**), ERG responses under conditions of light adaptation (**Fig.10a-d**) but not dark-adaptation [19], and visual behavior under photopic but not scotopic conditions (**Fig. 10e,f**). Together with the enlargement of synaptic sites, modest levels of synaptic release from cones of G369i KI mice may support nominal transmission of visual information through cone pathways. G369i KI mice could also exhibit homeostatic alterations in the inner retina, which are known to support visual function when photoreceptor input is severely compromised [33–35]. Future studies of the retinal circuitry and visual behavior of G369i KI mice could identify compensatory pathways that are recruited upon $Ca_V1.4$ loss-of-function and how they might be targeted in novel therapies for CSNB2 and related disorders.

Acknowledgements

J.W.M., G.J.O., J.D.V., A.H., K.R., and A.L. were supported by NIH grants EY026817 (to A.L.), EY029953 (to J.W.M.), and unrestricted funds from the University of Texas-Austin (to A.L.); S.R.W. and M.H. were supported by NIH grant EY031677 (to M.H.), an unrestricted grant from RPB to UW Madison Dept. of Ophthalmology and a McPherson ERI professorship to M.H.; D.F. and S.H.D. were supported by NIH grants EY012141 and EY032506, an unrestricted grant from RPB to the Northwestern University Dept. of Ophthalmology, and an RPB International Travel Award. N.A.S. and R.D. Mayfield were supported by AA029955 (N.A.S) and AA0012404 and AA020926 (R.D.M.). The authors thank J. Sun for assistance with acquiring some of the electrophysiological data in **Supp.Fig.S2**, S. Knecht and R. Wong for assistance with serial EM image collection, E. Seidemann and B. Shukla for the generous donation and collection of macaque retinal tissue, respectively, and M. McCall and F. Vinberg for advice on ERGs.

Author contributions

Conceptualization, J.W.M., G.O., A.L.; Methodology, J.W.M., G.O., J.D.V., A.L., M.H., S.H.D., D.F., N.S., R.D.M; Investigation, J.W.M., G.O., J.D.V., A.H., C.G., K.R., S.R.W., S.H.D., D.F.; Writing—original draft, A.L.; Writing—review and editing, J.W.M., G.J.O., M.H., S.H.D., A.L.; N.S., R.D.M. Funding acquisition, J.W.M., M.H., S.H.D., A.L., R.D.M.

Declaration of interests

The authors declare no competing interests.

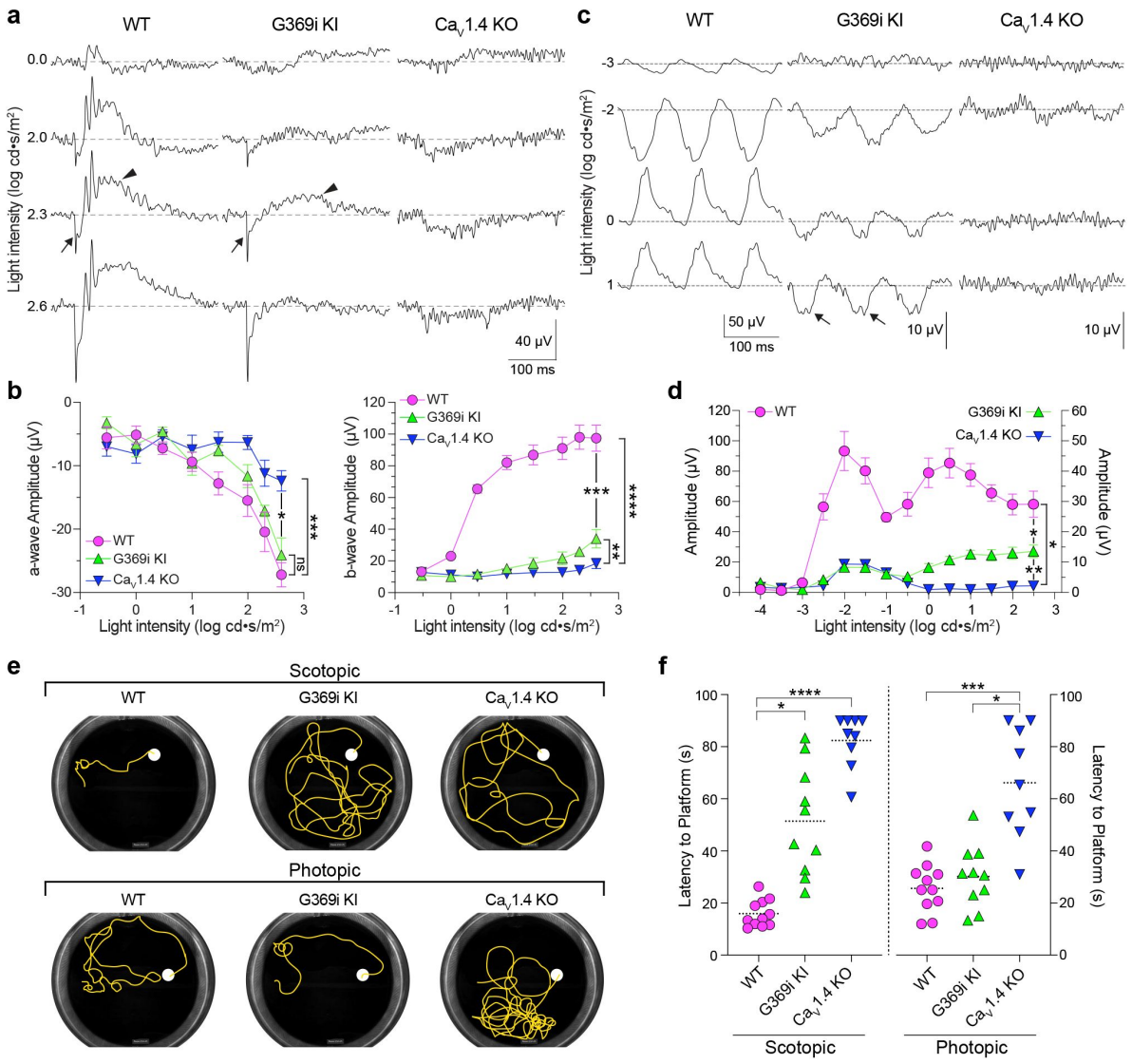

Figure 10.

Characterization of ERGs and visual behavior in WT, G369i KI, and $Ca_V1.4$ KO mice.

a, Representative traces of photopic ERGs recorded in the presence of background green light (20 cd · s/m^2) in WT, G369i KI and CaV1.4 KO mice. Flash intensities are shown at left. Arrows and arrowheads depict the a- and b-waves, respectively. ***b***, a-wave (left) and b-wave (right) amplitudes are plotted against light intensity. Symbols and bars represent mean ± SEM. WT, n = 7; G369i KI, n = 5; CaV1.4 KO, n = 6. *, p < 0.05; **, p < 0.01; ***, p < 0.001; ****, p < 0.0001; ns, not significant; Two-way ANOVA with Tukey's posthoc multiple comparisons. ***c,d***, Representative traces (*c*) and quantified data (*d*) for 10 Hz flicker responses evoked by white light flashes of increasing luminance (from −4 to 2 log cd· s/m^2). Arrows in *c* depict inverted waveform responses in G369i KI mice that are absent in Cav1.4 KO mice. Symbols and bars represent mean ± SEM. WT, n = 7; G369i KI, n = 5; CaV1.4 KO, n = 6. *, p < 0.05; **, p < 0.01. Two-way ANOVA with Tukey's posthoc multiple comparisons. ***e,*** Representative swim path traces of WT, G369i KI and CaV1.4 KO mice from the visible platform swim tests performed in the dark (scotopic, upper panel) and light (photopic, lower panel). ***f,*** Time required to reach the platform (latency to platform) was compared for each mouse strain. Symbols represent the average of the last 3 swim trials for each mouse of each genotype for both dark and light conditions. Dotted lines represent the mean. WT, n = 11; G369i KI, n = 10; CaV1.4 KO, n = 9. *, p < 0.05; ***, p < 0.001; ****, p < 0.0001; Kruskal-Wallis one-way ANOVA with Dunn's post hoc analysis.

Methods

Animals

All mouse and macaque experiments were performed in accordance with guidelines approved by the National Institutes of Health and the Institutional Animal Care and Use Committees at the University of Texas at Austin. All ground squirrel (*Ictidomys tridecemlineatus*) procedures performed at Northwestern University were approved by the Institutional Animal Care and Use Committee. The G369i KI [19] and $Ca_V1.4$ KO mouse strains were bred on the C57BL6/J background strain for at least 10 generations. Adult male and female mice were used (6-12 weeks old), and aged-matched C57BL6/J mice were used as the control (WT) animals.

Immunofluorescence

Mice between 6-8 weeks of age were anesthetized using isoflurane and euthanized by cervical dislocation. Eyes were enucleated and hemisected. The eye cups with retina were fixed on ice in 4% paraformaldehyde in 0.1 M phosphate buffer (PB) for 30 min. Fixed eye cups were then washed three times with 0.1 M PB containing 1% glycine followed by infusion of 30% sucrose at 4°C overnight. The eye cups were orientated along their dorsal-ventral axis and frozen in a 1:1 (wt/vol) mixture of Optimal Cutting Temperature compound and 30% sucrose in a dry ice/isopentane bath. Eye cups were cryosectioned at 20 µm on a Leica CM1850 cryostat (Leica Microsystems), mounted on Superfrost plus Micro Slides (VWR), dried for 5 to 10 min at 42°C, and stored at −20°C until used. Slides with mounted cryosections were warmed to room temperature, washed with 0.1 M PB for 30 min to remove the OCT/sucrose mixture and blocked with dilution solution (DS, 0.1 M PB/10% goat serum/0.5% Triton-X100) for 15 min or overnight at room temperature. All remaining steps were carried out at room temperature. All primary antibodies and appropriate secondary antibodies were diluted in DS at concentrations specified in the Key Resources Table (**Table 3**). Sections were incubated with primary antibodies for 1 h or overnight and then washed five times with 0.1 M PB. Sections were then incubated with secondary antibodies for 30 min and then washed five times with 0.1 M PB. Trace 0.1 M PB was removed, and sections were then mounted with #1.5H coverslips (ThorLabs) using ProLong Glass Antifade Mountant with or without NucBlue (Thermo Fisher Scientific).

For double labeling with other rabbit polyclonal antibodies, CAR antibodies were conjugated with the CF647 fluorophore (CAR-647) using the Mix-n-Stain antibody labeling kit according to the manufacturer's protocol (Biotium). Sections were processed first with rabbit polyclonal $Ca_V1.4$ or EAAT2 antibodies and corresponding secondary antibodies as described above. To prevent CAR-647 from binding to any available sites on the anti-rabbit secondary antibodies previously added to the sections, $Ca_V1.4$ or EAAT2 antibodies were readded to the sections and incubated for 30 min. After washing, the sections were incubated with CAR-647 for 1 h, followed by wash steps and cover glass mounting.

Immunofluorescence in labeled retinal sections was visualized using an Olympus FV3000 confocal microscope (Tokyo, Japan) equipped with an UPlanApo 60x oil HR objective (1.5 NA). Images were captured using the Olympus FLUOVIEW software package. Acquisition settings were optimized using a saturation mask to prevent signal saturation prior to collecting 16-bit. All confocal images presented are maximum z-projections. Images (256 x 256 pixels) used in analyses of synaptic proteins were collected using a 30X optical zoom, 0.6 Airy disk aperture, and voxel size of 0.028 μm × 0.028 μm × 0.2 μm ($X \times Y \times Z$). Amira segmentation was used for generating 3D binary masks, and Amira 3D label analysis was used for quantification of immunofluorescent and masked images. Non-deconvolved images were used for all analyses. 3D binary masks of individual CAR-labeled pedicles were made by setting the threshold 1 standard deviation above mean fluorescence intensity of each 3D image. 3D binary masks of presynaptic labels (CtBP2, $Ca_V1.4$, and Bassoon) or

Primary Antibodies				
Antibody Name (clone/designation)	**Working Concentration**	**Source**	**Identifier**	**RRID**
Bassoon (SAP7F407/Ms monoclonal)	2 µg/mL	ThermoFisher Scientific	MA1-20689	AB_2066981
$Ca_V1.4$ (Rb Polyclonal)	5 µg/mL	Amy Lee	Ab167	AB_2650487
Cone Arrestin (Rb Polyclonal)	1 µg/mL	Millipore	AB15282	AB_1163387

Table 3.

Key resources used in this study.

Cone Arrestin-CF647 (Rb Polyclonal)	5 µg/mL	Millipore	AB15282	AB_1163387
CtBP2 (Clone 16/Ms Monoclonal)	1 µg/mL	BD Biosciences	612044	AB_399431
GPR179 (mAB 1a/Ms Monoclonal)	2 µg/mL	Millipore	MAB427	AB_2069582
mGluR6 (366/Ms Monoclonal)	1 µg/mL	Dr. Theodore Wensel (Agosto et al., 2014, 2018)	N/A	N/A
TRPM1 (545H5/Ms Monoclonal)	1 µg/mL	Dr. Theodore Wensel (Agosto et al., 2018)	N/A	N/A
Secondary Antibodies				
Antibody Name and Conjugate	**Working Concentration**	**Source**	**Identifier**	**RRID**
Goat Anti-Mouse IgG1 Alexa Fluor 488	4 µg/mL	ThermoFisher	A-21121	AB_2535764
Goat Anti-Mouse IgG2a Alexa Fluor 555	4 µg/mL	ThermoFisher	A-21137	AB_2535776
Goat Anti-Rabbit Alexa Fluor 555	4 µg/mL	ThermoFisher	A-21429	AB_2535850
Goat Anti-Rabbit Alexa Fluor 647	4 µg/mL	ThermoFisher	A-21245	AB_2535813

Chemicals		
Reagent or Resource	**Source**	**Identifier**
Adenosine 5'-triphosphate magnesium salt	SIGMA	A9187
Agarose, low gelling temperature	Sigma-Aldrich	A0701
AMES	Sigma, US Biological	Sigma: A1420; US Biological: A1372
Antisedan	Zoetis US LLC	10000449
1,2-Bis(2-aminophenoxy)ethane-N,N,N′,N′-tetraacetic acid (BAPTA)	Sigma-Aldrich	A4926
Cadmium Chloride	Sigma	202908
Calcium chloride dihydrate	Sigma-Aldrich	223506
Cesium Chloride	Fisher Bioreagents	BP210
Cesium methanesulfonate	Sigma-Aldrich	C1426
Creatine phosphate, dipotassium salt	EMD Millipore	237911
D-Glucose	Fisher	D16
DL-*threo*-β-Benzyloxyaspartic acid (DL-TBOA)	Tocris	1223
6,7-Dinitroquinoxaline-2,3-dione disodium salt (DNQX)	Abcam	ab120169
Dimethyl sulfoxide	SIGMA	D2650
Dulbecco's Modified Eagle Medium, high glucose	Gibco	11965-092
Dulbecco's Phosphate Buffered Saline, no calcium, no magnesium	Gibco	14190-144
Ethylene glycol-bis(2-aminoethylether)-N,N,N',N'-tetraacetic acid (EGTA)	Sigma-Aldrich	03777
Fetal Bovine Serum (FBS)	Gibco	16140-071
FuGENE HD Transfection reagent	Promega	E2311
Guanosine 5'-triphosphate sodium salt hydrate	Sigma-Aldrich	G8877
4-(2-Hydroxyethyl)piperazine-1-ethanesulfonic acid (HEPES)	SIGMA	H3375
Systane Hypromellose lubricant eye gel	Alcone	300650474016
Isradipine	Sigma-Aldrich	I6658
Ketamine Injection C IIIN 100 mg/mL	Dechra Veterinary Products, LLC	17033-100-10

Table 3. (continued)

Table 3. (continued)

Magnesium Chloride hexahydrate	SIGMA	M2393
Methanesulfonic acid	Sigma-Aldrich	471356
Mix-n-Stain Antibody Labeling Kit	Biotium	92238
ML218 Hydrochloride	Tocris	4507
N-Methyl-D-glucamine (NMDG)	Sigma-Aldrich	66930
Nickel Chloride	Sigma	339350
Optimal Cutting Temperature compound	Sakura	4583
Penicillin-Streptomycin	Sigma-Aldrich	P0781
Picrotoxin	Tocris	1128
Sigmacote	Sigma-Aldrich	SL2-25mL
Sodium Bicarbonate	MACRON	7412-12
Sodium phosphate monobasic anhydrous	Sigma	S3139
Sodium phosphate dibasic anhydrous	Sigma	RDD022
Sodium Chloride, Crystal	MACRON	7581-12
Potassium Chloride	Fisher Chemical	P217
Sodium hydroxide	Fisher chemical	S318
Sodium lactate	Sigma-Aldrich	1614308
Sodium malate	Sigma-Aldrich	1613881
Sodium pyruvate	Sigma-Aldrich	P2256
Sodium succinate	Sigma-Aldrich	S9637
Strychnine HCl	Sigma	S8753
(3*S*)-3-[[3-[[4-(Trifluoromethyl)benzoyl]amino]phenyl]methoxy]-L-aspartic acid (TBF-TBOA)	Tocris	2532
Tetraethylammonium chloride (TEA-Cl)	Sigma-Aldrich	86614
TRIS	VWR	0497
Tropicamide ophthalmic solution 1%	Akorn, Inc.	17478-0102-12
Trypsin-EDTA (0.05%), phenol red	Gibco	25300054
Anased (Xylazine) Injection 100 mg/mL	Pivetal	46066-0750-02
4-Ethylphenylamino-1,2-dimethyl-6-methylaminopyrimidinium chloride (ZD7288)	Tocris	1000

Experimental Models: Organisms/Strains

Reagent or Resource	Source	Identifier	RRID
HEK293T	ATCC	CRL-3216	CVCL_0063
Mouse: C57BL/6J	Jackson Labs	000664	IMSR_JAX:000664
Mouse: G369i KI	A. Lee [19]	N/A	N/A
Mouse: $Ca_V1.4$ KO	Jackson Labs	017761	IMSR_JAX:017761
Ground Squirrel	TLC	--	--

Software and Algorithms

Reagent or Resource	Source	Identifier
Amira	ThermoFisher Scientific	https://www.thermofisher.com/amira
cellSens	Olympus	https://www.olympus-lifescience.com/en/software/cellsens
Espion software	Diagnosys, Inc.	https://info.diagnosysllc.com/software
FLUOVIEW	Olympus	https://www.olympus-lifescience.com/en/laser-scanning/fv3000
GraphPad Prism	GraphPad	https://www.graphpad.com
IGOR Pro	WaveMetrics	https://www.wavemetrics.com
ImageJ	NIH	https://imagej.nih.gov/ij
pClamp	Molecular Devices	https://www.moleculardevices.com
Patchmaster	Harvard Bioscience, Inc.	https://www.heka.com
ScanImage	MBF Biosciences	https://docs.scanimage.org/index.html

postsynaptic labels (GPR179, mGluR6, and TRPM1) within or associated with the pedicle, respectively, were made by setting the threshold 3 standard deviations above the mean fluorescence intensity. To aid in presentation, high-mag images displayed in **Figs.1b** and **6a** were deconvolved using cellSens software (Olympus), and any immunofluorescence corresponding to rod synaptic proteins was subtracted from the image.

Molecular biology and transfection

The cDNAs for $Ca_V1.4$ (GenBank: NM_019582), β_{2X13} (GenBank: KJ789960), and $\alpha_2\delta$-4 (GenBank: NM_172364) were previously cloned into pcDNA3.1 [66]. The cDNA for $Ca_V3.2$ (GenBank: AF051946) was a gift from Dr. Edward Perez-Reyes, University of Virginia. All constructs were verified by DNA sequencing before use. Human embryonic kidney 293T (HEK293T) cells were cultured in Dulbecco's Modified Eagle's Medium with 10% FBS at 37°C in 5% CO_2. At 70–80% confluence, the cells were co-transfected with cDNAs encoding human $Ca_v1.4$ (1.8 µg) β_{2X13} (0.6 µg), $\alpha_2\delta$-4 (0.6 µg), and enhanced GFP in pEGFP-C1 (Clonetech, 0.1 µg) or $Ca_V3.2$ (2 µg) and pEGFP-C1 (0.1 µg) using FuGENE 6 transfection reagent according to the manufacturer's protocol. Cells treated with the transfection mixture were incubated at 37°C for 24 hr, dissociated using Trypsin-EDTA, and replated at a low density to isolate single cells. Replated cells were then incubated at 30°C or 37°C for an additional 24 hr before beginning experiments.

Solutions for patch clamp recordings

HEK293T extracellular recording solution contained the following (in mM): 140 Tris, 20 $CaCl_2$, 1 $MgCl_2$, pH 7.3 with methanesulfonic acid, osmolarity 309 mOsm/kg. HEK293T internal recording solution contained the following: 140 NMDG, 10 HEPES, 2 $MgCl_2$, 2 Mg-ATP, 5 EGTA, pH 7.3 with methanesulfonic acid, osmolarity 358 mOsm/kg.

For recordings of I_{Ca} in mouse retina, extracellular recording solution contained the following (in mM): 115 NaCl, 2.5 KCl, 22.5 $NaHCO_3$, 1.25 NaH_2PO_4, 2 $CaCl_2$, 1 $MgCl_2$, 5 HEPES, CsCl, 5.5 Glucose, osmolarity 290 mOsm/kg. Mouse cone intracellular solution contained the following (in mM): 105 $CsMeSO_4$, 20 TEA-Cl, 1 $MgCl_2$, 11 HEPES, 10 EGTA, 4 Mg-ATP, 10 phosphocreatine, 0.3 Na-GTP, pH 7.4 with CsOH, osmolarity 300 mOsm/kg.

For recordings of I_{Ca} in ground squirrel retina, extracellular recording solution contained the following (in mM): 10 HEPES, 85 NaCl, 3.1 KCl, 2.48 $MgSO_4$, 6 Glucose, 1 Na-succinate, 1 Na-malate, 1 Na-lactate, 1 Na-pyruvate, 2 $CaCl_2$, 25 $NaHCO_3$, and 20 TEA-Cl, osmolarity 285 ± 5 mOsm/kg. Intracellular solution contained the following (in mM): 80 CsCl, 10 BAPTA, 2 $MgSO_4$, 10 HEPES, 20 TEA-Cl, 5 Mg-ATP, and 0.5 Na-GTP, pH 7.35 with CsOH, osmolarity 285 ± 5 mOsm/kg. For recordings of I_{Aglu}, extracellular recording solution contained (in mM): 125 NaCl, 3.0 KCl, 1.25 NaH_2PO_4, 25 $NaHCO_3$, 2 $CaCl_2$, 1 $MgCl_2$, 3 dextrose, 3 sodium pyruvate, 0.1 picrotoxin and 0.02 DNQX, and in indicated experiments 0.0013 TFB-TBOA. Intracellular I_{Aglu} contained (in mM): 125 KSCN, 10 TEA-Cl, 10 HEPES, 1 $CaCl_2$, 2 $MgCl_2$, 0.3 Na-GTP, 4 Mg-ATP, 10 K_2 phosphocreatine, 0.02 ZD7288. Mouse and ground squirrel extracellular slice recording solutions were equilibrated with 5% CO_2 / 95% O_2 to a pH of ~7.5.

For recordings of light responses in horizontal cells of mouse retina, extracellular recording solution consisted of Ames' media supplemented with 100 U/mL penicillin, 0.1 mg/mL streptomycin and 22.6 mM $NaHCO_3$, osmolarity 280 ± 5 mOsm/kg. The intracellular recording solution contained the following (in mM): 135 K-Aspartate, 10 KCl, 10 HEPES, 5 EDTA, 0.5 $CaCl_2$, 1 Mg-ATP, 0.2 Na-GTP, pH 7.35 with KOH, osmolarity 305 ± 5 mOsm/kg.

Patch clamp electrophysiology

Whole-cell voltage clamp recordings of transfected HEK293T cells were performed 48 to 72 hrs after transfection using an EPC-10 amplifier and Patchmaster software (HEKA Elektronik, Lambrecht, Germany). Patch pipette electrodes with a tip resistance between 4 and 6 MΩ were pulled from thin-walled borosilicate glass capillaries (World Precision Instruments, Sarasota, FL) using a P-97 Flaming/Brown Puller (Sutter Instruments, Novato, CA). A reference Ag/AgCl wire was placed into the culture dish mounted on an inverted Olympus IX70 microscope. Recordings were performed at room temperature. A pressurized perfusion pencil multi-barrel manifold controlled with Valve Bank II (AutoMate Scientific, Inc., Berkeley, CA) was used to deliver extracellular solutions. ML218 of different concentrations (0.5, 1, 5, 25 and 100 mM) was added to the extracellular solution the day of experiments. Series resistance was compensated up to 70%, and passive membrane leak subtraction was conducted using a P/−4 protocol. Whole-cell Ca^{2+} currents (I_{Ca}) of transfected HEK293T cells were evoked for 50 ms with incremental +5 mV steps from −80 mV to +65 mV. Current-Voltage (IV) data were fit with a single Boltzmann equation: $I_{Ca} = G_{max}(V_m - V_r)/(1+\exp[-(V_m-V_h))/k])$, where G_{max} is the maximal conductance, V_m is the test voltage, V_r is the Ca^{2+} reversal potential, V_h is the membrane potential required to activate 50% of G_{max}, and k is the slope factor. Data were sampled at 100 kHz, filtered at 3 kHz, and analyzed using custom programs written in IgroPro (WaveMetrics).

Whole-cell voltage clamp recordings of mouse cones, macaque cone terminals, and mouse horizontal cells were performed using an EPC-10 amplifier and Patchmaster software (HEKA). Patch pipette electrodes with a tip resistance between 10 and 14 MΩ for cones and 6-8 for horizontal cells were pulled from thick-walled borosilicate glass (1.5 mm outer diameter; 0.84 mm inner diameter; World Precision Instruments).

To prepare retinal slices, adult mice (6 – 8 weeks old) were anesthetized using isoflurane and euthanized by cervical dislocation. Eyes were enucleated, placed into cold Ames' media slicing solution, and hemisected. Following removal of the vitreous, the eye cup was separated into dorsal and ventral halves using a scalpel. Ventral retina was isolated, molded into low-melt agarose and mounted in a Leica VT1200s vibratome (Leica Biosystems). Mouse retina slicing solution was continuously bubbled with 100% O_2 and contained the following: Ames' Medium with L-glutamine supplemented with (in mM) 15 NaCl, 10 HEPES, 10 U/mL penicillin, 0.1 mg/mL streptomycin, pH 7.4, osmolarity 300 mOsm/kg. Vertical (~200 µm) or horizontal (~160 µm) retinal slices were anchored in a recording chamber, placed onto a fixed stage, and positioned under an upright Olympus BX51WI microscope equipped with a 60X water-immersion objective (1.0 NA), and superfused with extracellular solution (flow rate of ~1-2 ml/min) at room temperature. Slices were visualized using IR-DIC optics and an IR-2000 (Dage MTI, Michigan City, IN) or SciCam Pro (Scientifica, Uckfield, United Kingdom) CCD camera controlled by the IR-capture software package or µManager, respectively [67], [68]. Drugs used in these experiments were added to the mouse extracellular solution the day of experiments at the concentration described in **Table 4**. A reference Ag/AgCl pellet electrode was placed directly into the recording chamber solution. Data from whole-cell recordings with a series resistance >20 MΩ were discarded.

Cone somas were identified based on their morphology and location (outer ONL cell layer). Cone identity was confirmed by the whole-cell capacitance (~3-4 pF), which is larger than rod whole-cell capacitance (~0.7-1 pF). For cone voltage ramp recordings, cones were held at - 90 mV for 200 ms followed by a ramp of +0.5 mV/ms to +40 mV. To determine voltage activation of I_{Ca}, whole-cell Ca^{2+} currents in cones were evoked for 50 ms with incremental +5 mV steps from −80 mV to +40 mV. The activation voltage of I_{Ca} is reported as G/G_{max}, where G is the conductance at each test voltage and G_{max} is the maximum peak conductance for each cone.

Table 4.

Pharmacological drugs and their concentrations used in electrophysiological recordings of cones.

Compound	Concentration (μM) for mouse recordings	Concentration (μM) for ground squirrel recordings
Cadmium	200	N/A
DL-TBOA	N/A	375
DNQX	20	N/A
Isradipine	1	2
ML218	5	5
Nickel	100	N/A
Picrotoxin	N/A	50
Strychnine	N/A	10
ZD7288	N/A	50
Glutamate	1000	N/A

Conductance was calculated using the equation I_{Ca} = G(V_m-V_r), where V_r is +60 mV. To determine steady state inactivation of I_{Ca}, currents in cones were evoked for 500 ms with incremental +5 mV steps from −90 mV and −30 mV followed by a final step to −30 mV for 50 ms after each test voltage. The steady state inactivation of I_{Ca} is reported as I/I_{max}, where I is the peak current in the final voltage step to −30 mV and I_{max} is the maximum peak current for each cone. Data were sampled between 20 and 60 kHz and filtered at 3 kHz.

For horizontal cell light responses, horizontal slices were prepared from central mouse retina. The identity of horizontal cells was determined based on their larger soma diameter (~15 µm) compared to bipolar cell somas (~6 µm). During whole cell patch clamp recordings, horizontal cells were held at −70 mV. Light stimuli (1 s) at 410 nm (630 x 830 µm) were presented onto the retina (at a minimum of 5 s intervals) through the microscope's condenser using a Polygon1000 DMD pattern illuminator (Mightex, Pleasanton, CA, USA) and a custom-built light path. Light intensity (in watts) was measured at the point on the microscope stage where the retina is placed using a power meter (Thorlabs, Newton, New Jersey, USA). Photon flux Φ_q (photons/s) within the light stimulus area was calculated using the measured light intensities in the formula:

$$\Phi_q \text{ per } \mu m^2 = \frac{measured\ light\ intensity\ (W)}{\frac{hc}{\lambda}} / light\ stimulus\ area\ (\mu m^2)$$

where h is Planck's constant (J*s), c is the speed of light (m/s), and λ is the wavelength (m). Light stimulus intensity was increased in Log2 steps from 4.9×10^2 to 2.1×10^5 $\Phi_q/\mu m^2$. For each light intensity step, both ON and OFF current amplitudes were measured from baseline (averaged 5 ms of current prior to light onset) to the maximum positive (after light onset) or maximum negative (after light offset) current, respectively. To confirm the identity of these horizontal cell light responses as AMPA-mediated currents, 1 s light stimuli (410 nm, 1.2×10^5 $\Phi_q/\mu m^2$) were continuously delivered every 10 s before, during and after bath application of 20 µM DNQX.

For voltage clamp recordings of 13-lined ground squirrel cones, retinal slices were prepared as previously described [69]. The eyecup was divided along the dorsal to ventral axis into superior, middle, and inferior parts. The dorsal area above the line of the optic nerve head was defined as superior, the central region with a width of about 5 mm just ventral to the optic nerve head was middle, and the remaining ventral area was inferior. Isradipine and ML218, alone or in combination, were applied from separate puffer pipettes whose orifices were aimed at the cone synaptic region. Recordings were made with an Axopatch 200B amplifier (Molecular Devices). Signals were electronically filtered at 5 kHz and digitized at a rate of 10 kHz. Additional Gaussian filtering was added (cutoff frequency of 500 Hz). Tissue was viewed through a 63x water immersion objective on a Zeiss Axioskop FS2 microscope and superfused with extracellular solution at room temperature. Drugs and their concentrations used during these experiments are described in **Table 4**. Membrane potential was continuously maintained at −85 mV. During ramp stimulation, the membrane potential was depolarized to −85 to +35 mV at a rate of 1 mV/ms.

For rhesus macaque cone terminal recordings, a 12-year-old male was sedated with ketamine (5 mg/kg I.M.) and dexmedetomidine (0.015 mg/kg I.M.). Post-sedation, the animal received buprenorphine (0.02 mg/kg I.M.), atropine (0.02 mg/kg I.M.), and maropitant citrate (1 mg/kg S.Q.). The animal was intubated and maintained with inhaled isoflurane (0.75-2.0%) and propofol (7-8 mg/kg/hr I.V.). Crystalloid fluids (5 mL/kg/hr) were administered I.V., and phenylephrine (5-10 mcg/kg/hr I.V.) was used for blood pressure support. The animal was under anesthesia for approximately 3 hours prior to perfusion. Transcardial perfusion was approached through a midline thoracotomy. Immediately prior to perfusion, 5 mL of Euthasol® (sodium pentobarbital 390 mg/mL/phenytoin sodium 50 mg/mL) was administered I.V. The descending thoracic aorta was clamped, the pericardium was opened, and the right atrium was cut. The apex of the left ventricle was sharply incised, and a large bore cannula (Yankauer suction handle, 5 mm internal diameter) was inserted through the left ventricle until it could be palpated in the ascending aorta. The

cannula was clamped in place at the apex of the left ventricle. The animal was perfused with 4 L of cold phosphate-buffered saline at ~500 mL/min. Eyes were removed approximately 1 hour following perfusion. Eyes were dissected, and eye cups were allowed to dark adapt for ~30 min and stored in bicarbonate buffered Ames' media at 32°C equilibrated with 95% O_2/5% CO_2 prior to slice preparations. Vertical sections of central retina were prepared from 5 mm retina punches as described for mice.

Single cell RNA sequencing

Retinas from 2 WT and 2 G369i KI mice (2-3 month old, all males) were dissected in ice-cold Dulbecco's Phosphate Buffered Saline (D-PBS) and dissociated into single cells using the Papain Dissociation System (Worthington Biochemical). Two retinas were incubated in a 2.5 ml of dissociation solution (40 U/ml papain, 2 mM L-cysteine, 200 U/ml DNAse in Earle's Balanced Salt Solution, EBSS) for 8 min at 37 °C. Following aspiration, 2 ml of inactivation solution (ovomucoid protease inhibitor and bovine serum albumin (BSA), 10 mg/ml each in EBSS) was added prior to trituration with a series of fire-polished, siliconized glass Pasteur pipettes. The solution was passed through a 40 µm mesh (pluriStrainer, Cat# 43-50040-51, pluriSelect) prior to centrifugation (200 x *g* for 5 min, 4 °C). Following aspiration of the supernatant, the cell pellet was resuspended in 0.5 ml D-PBS+0.5% BSA. Cell suspensions (10,000 cells per sample) were loaded on the Chromium Controller (10X Genomics) and processed for cDNA library generation following the manufacturer's instructions for the Chromium NextGEM Single Cell 3' Reagent Kit v3.1 (10X Genomics). The resulting libraries were examined for size and quality using the Bioanalyzer High Sensitivity DNA Kit (Agilent) and their concentrations were measured using the KAPA SYBR Fast qPCR kit (Roche). Samples were sequenced on the NovaSeq 6000 instrument (paired end, read 1: 28 cycles, read 2: 90 cycles) with a targeted depth of 9K reads/cell.

scRNA-seq Fastq files were processed with CellRanger (v7.1.0) using the reference genome mm10–2020-A with introns included. CellRanger outputs were imported to Seurat (v5.0.1), gene by feature count matrix was constructed, log normalization was performed, and the log normalized values were used for downstream analysis. Unsupervised clustering was performed in Seurat using resolution=0.5. DEsingle method (v1.6.0, [70]) was used for differential expression analysis comparing G369i KI to WT in each cluster.

Serial block-face scanning electron microscopy and 3D reconstructions

Eye cups were prepared from P42 WT and G369i KI littermates and fixed using 4% glutaraldehyde in 0.1M cacodylate buffer, pH 7.4, for 4 hours at room temperature followed by additional fixation overnight at 4°C. Glutaraldehyde-fixed eye cups were then washed 3 times in 0.1M cacodylate buffer. Retinas were thereafter isolated and embedded in Durcupan resin after staining, dehydration, and embedding as described previously (Della Santina et al., 2016). A Thermo Scientific VolumeScope serial block face scanning electron micrscope was used to image embedded retinas. Retinal regions comprising a 2×2 montage of 40.96 µm tiles were imaged at a resolution of 5nm/pixel and section thickness of 50 nm. Image stacks were aligned, and cone photoreceptor terminals reconstructed using TrakEM2 (NIH). Postsynaptic partners at cone ribbons were followed to the inner nuclear layer to determine their identity. Amira software was used for 3D visualization of reconstructed profiles.

Electroretinography

Retinal function was assessed using the Celeris system (Diagnosys, Inc.) paired with the Espion software (Diagnosys, Inc.). Mice were anaesthetized under red light (660 nm) via intraperitoneal (I.P.) injection with ketamine/xylazine mixture (100 mg/kg ketamine, 10 mg/kg xylazine). Tropicamide ophthalmic solution (1 %) and hypromellose lubricant eye gel (0.3 %) were administered topically to both eyes before the mouse was secured to a heated (37 °C) platform to

maintain body temperature. Ag/AgCl corneal stimulators were placed on each eye. After collecting data from individual mice, atipamezole (Antisedan, 1-2 mg/kg) was I.P. injection administered to reverse the effects of the ketamine and xylazine. For photopic ERGs, eyes were light adapted using a background green light at 20 cd·s/m^2 for 10 min. Following light adaptation, eight different light intensity pulses (−0.5, 0, 0.5, 1, 1.5, 2, 2.3 and 2.6 log cd·s/m^2) were delivered on top of the background green light. ERG a-waves were measured from baseline to the peak of the negative potential. ERG b-waves were measured without filtering the oscillatory potentials from the peak of the a-wave to the peak of the positive potential within 60-70 ms (WT) and 80-100 ms (G369i KI and $Ca_V1.4$ KO) of the light stimuli. For flickering ERGs, mice were dark adapted (>12 h). White light pulses from −4 to 2.5 log cd·s/m^2 were delivered in 0.5 log unit steps at 10 Hz. Response amplitudes were measured from the trough to the peak of each response at all light intensities. Each intensity stimulus was delivered 10 times, with a 3 s interval between each stimulus, and averaged. The mean response amplitudes recorded in the right and left eye of each mouse are reported for all quantified ERG data.

Visible platform swim test

The visible platform swim test was performed as has been previously described [31]. WT, G369i KI, and $Ca_V1.4$ KO male and female mice (6-9 weeks old) were dark-adapted overnight and allowed to adapt to the procedure room for at least 1 h prior to beginning the experiments. A water-filled, 4-foot diameter galvanized steel tank and a visible white platform with a diameter of 10 cm was used for the swim test. Mice were subjected to 6 swim trials per day. Assays conducted under photopic (55 lux) and scotopic conditions (0 lux) were performed on days 1 and 2, respectively. Light intensity for photopic and scotopic conditions was measured at the platform using an Extech HD450 light meter (FLIR Systems, Nashua, New Hampshire). Mice were given 90 s to find the platform before being removed. After one trial was performed on all mice, the platform was moved to one of three different locations, top left, top center, and top right in relation to the initial site of mouse placement in tank. Each trial was recorded using an infrared camera (Basler AG, Ahrensburg, Germany) and EthoVision XT16 software (Noldus Information Technology). Locating the platform was considered successful when mice contacted the platform with a head-on approach, even if mice failed to escape onto the platform. Mice were allowed to rest on the platform for 15 s at the end of each trial before being returned to a pre-warmed cage. Latency to find the platform was manually recorded and confirmed using recorded videos. Male and female mice were tested separately, and no sex differences in performance were identified post-hoc using two-way RM-ANOVA (**Supplementary Table 1**). Male and female data were combined into a single group for each genotype. Latency to platform was calculated by averaging the final 3 trials under scotopic and photopic conditions for each mouse and compared using Kruskal-Wallis one-way ANOVA with Dunn's posthoc multiple comparison test.

Ca^{2+} Imaging of Cone Terminals

Retinas were dissected and stored in oxygenated mouse retina slicing solution. The loading of the cell-permeant Ca^{2+} dye Fluo-3, AM was modified from on a previous publication[71]. To label the base of cone terminals, retinas were incubated in retina slicing solution containing PNA Lectin conjugated with CF568 (100 μg/mL) for 15 min at room temperature. Then the retinas were incubated with retina slicing solution containing 1mM Fluo-3, AM and 0.025% pluronic acid (Biotium) for 45 min at room temperature followed by 3 rinses with retina slicing solution. The retinas were then incubated in retina slicing solution for 15 min at 35°C to increase esterase activity. Vertical retina slices were prepared as described above. Slices were mounted on a Hyperscope multiphoton system (Scientifica, Uckfield, United Kingdom) equipped with a resonant scanner and a Mai Tai HP DeepSee laser (Spectra-Physics, Milpitas, CA, USA) tuned to 800 nm at 5% power. Slices were perfused with normal extracellular solution containing (in mM) 112 NaCl, 3 KCl, 1 $MgCl_2$, 3 $CaCl_2$, 1.25 NaH_2PO_4, 10 Na Pyruvate, 22.5 $NaHCO_3$, 5 HEPES, 10 Glucose, osmolarity 300 ± 5 mOsm/kg. High-K+ extracellular solution contained (in mM) 65 NaCl, 50 KCl, 1 $MgCl_2$, 3 $CaCl_2$, 1.25 NaH_2PO_4, 10 Na Pyruvate, 22.5 $NaHCO_3$, 5 HEPES, 10 Glucose, osmolarity 300 ± 5

mOsm/kg. Extracellular solutions were supplemented with 20 μM CNQX, 25 μM L-APV, and 100 μM picrotoxin. Isradipine (10 μM) was added to High-K+ extracellular solution. Images (512×512) were collected as 15-frame averages at 0.93 Hz using ScanImage (MBF Bioscience, Williston, VT, USA). Changes of Fluo-3 fluorescence in cone terminals were measured in ROIs drawn juxtaposed to PNA-CF568 labeling using Fiji[72].

Data analysis

Electrophysiological data were analyzed by custom routines written in IgorPro software (Wavemetrics) and statistical analysis was performed using Prism software (GraphPad). Data were analyzed for normality by Shapiro Wilk test followed by parametric (t-test or ANOVA) or non-parametric methods (Kruskal Wallis, Mann-Whitney, Wilcoxon).

Male versus Female WT (Photopic)	SS	DF	MS	F (DFn, DFd)	P value
Trial x Genotype	1125	5	224.9	F (5, 45) = 0.6060	P=0.6956
Trial	3564	5	712.9	F (5, 45) = 1.921	P=0.1096
Genotype	273.6	1	273.6	F (1, 9) = 0.6616	P=0.4370
Subject	3722	9	413.5	F (9, 45) = 1.114	P=0.3727
Residual	16703	45	371.2		
Male versus Female G369i KI (Photopic)	SS	DF	MS	F (DFn, DFd)	P value
Trial x Genotype	1457	5	291.4	F (5, 45) = 0.5362	P=0.7477
Trial	3516	5	703.2	F (5, 45) = 1.294	P=0.2833
Genotype	1150	1	1150	F (1, 9) = 0.8168	P=0.3897
Subject	12675	9	1408	F (9, 45) = 2.592	P=0.0168
Residual	24451	45	543.4		
Male versus Female Cav1.4 KO (Photopic)	SS	DF	MS	F (DFn, DFd)	P value
Trial x Genotype	1736	5	347.1	F (5, 35) = 0.6597	P=0.6563
Trial	993	5	198.6	F (3.056, 21.39) = 0.3775	P=0.7737
Genotype	78.37	1	78.37	F (1, 7) = 0.03788	P=0.8512
Subject	14481	7	2069	F (7, 35) = 3.932	P=0.0029
Residual	18416	35	526.2		
Male versus Female WT (Scotopic)	SS	DF	MS	F (DFn, DFd)	P value
Trial x Genotype	862	5	172.4	F (5, 45) = 0.6907	P=0.6331
Trial	914.5	5	182.9	F (5, 45) = 0.7328	P=0.6027
Genotype	634.7	1	634.7	F (1, 9) = 2.121	P=0.1793
Subject	2693	9	299.3	F (9, 45) = 1.199	P=0.3193
Residual	11232	45	249.6		
Male versus Female G369i KI (Scotopic)	SS	DF	MS	F (DFn, DFd)	P value
Trial x Genotype	7648	5	1530	F (5, 45) = 2.581	P=0.0390
Trial	1644	5	328.8	F (5, 45) = 0.5547	P=0.7339
Genotype	4712	1	4712	F (1, 9) = 4.716	P=0.0580
Subject	8993	9	999.2	F (9, 45) = 1.686	P=0.1206
Residual	26671	45	592.7		
Male versus Female Cav1.4 KO (Scotopic)	SS	DF	MS	F (DFn, DFd)	P value
Trial x Genotype	1727	5	345.4	F (5, 35) = 1.470	P=0.2246
Trial	12215	5	2443	F (2.802, 19.62) = 10.40	P=0.0003
Genotype	96.33	1	96.33	F (1, 7) = 0.1346	P=0.7246
Subject	5011	7	715.9	F (7, 35) = 3.046	P=0.0131
Residual	8225	35	235		

Data were analyzed by two-way repeated measures ANOVA. SS, sums of squares; DF, degrees of freedom; MS, mean square; F(DFn, DFd), F statistic.

Supplementary Table 1.

Statistical analysis of visible platform swim test disaggregated by sex

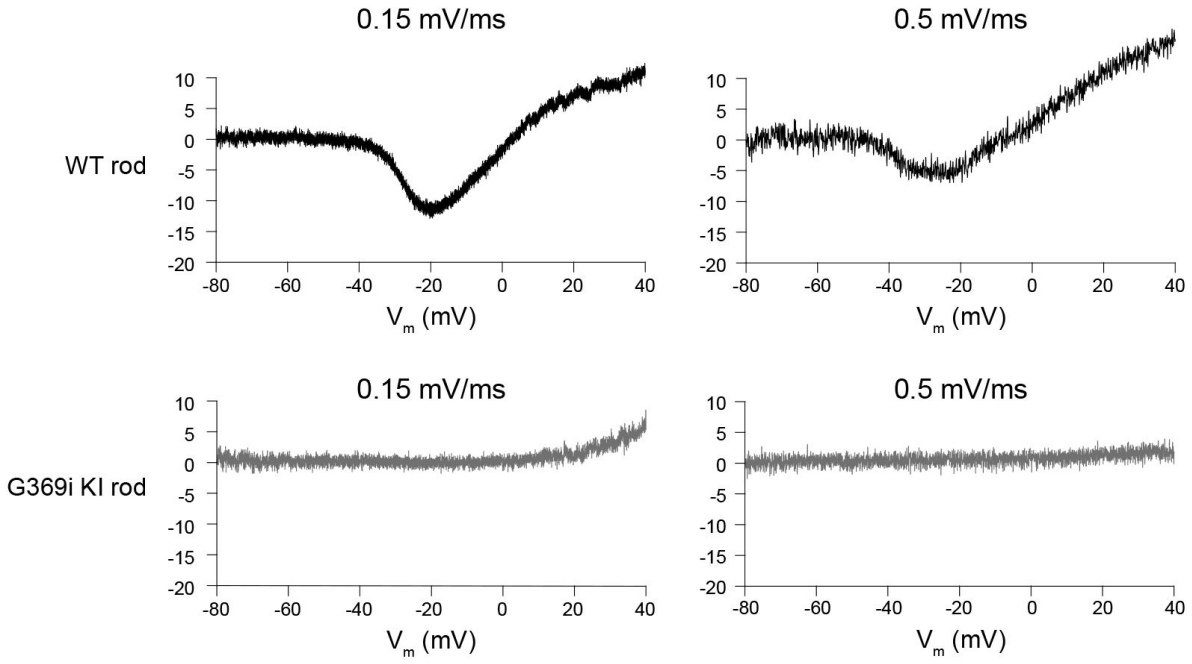

Supplementary Figure S1.

Voltage ramps do not reveal I_{Ca} in rods of G369i KI mice.

I_{Ca} was evoked by voltage ramps at 0.15 mV/ms or 0.5 mV/ms in rods of WT or G369i KI mice.

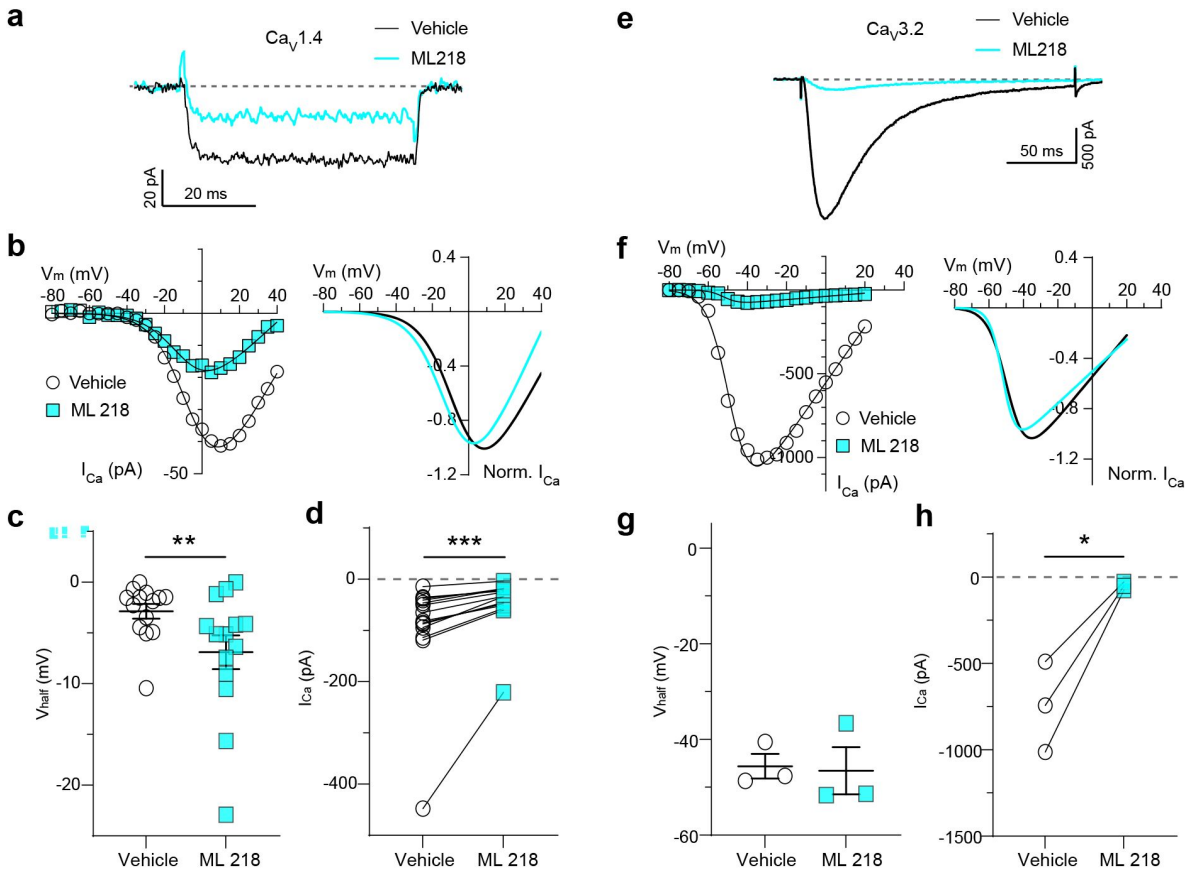

Supplementary Figure S2.

Effect of 218 on Ca$_V$1.4 and Ca$_V$3.2 in EK293T cells.

Cells were transfected with Ca$_V$1.4, 2×13, and 2 4 (a d) or Ca$_V$3.2 (e h). ***a,e***, epresentative traces and I V plots for I_{Ca} evoked by 50 ms steps to 10 mV (a) or 200 ms steps to 35 mV (e) from a holding voltage of 90 mV. Currents were recorded in the presence of vehicle (SO) or 218 (5 for Ca$_V$1.4 and 1 for Ca$_V$3.2). ***b,f***, eft, I V relationships for data obtained as in *a,e* but using steps to various voltages from a single representative cell. ight, olt mann fit of the responses, normali ed to the maximum I_{Ca} amplitude. ***c,d,g,h***, Graphs depicting effect of 218 on Vhalf (c,g) and I_{Ca}. ** W= 93.00, = 3.1366, p=0.001 *** W=105.0, =3.8419, p=0.0001 both by Wilcoxon matched pairs signed rank test. * t(2)=0.582, p=0.0366 by paired t test.

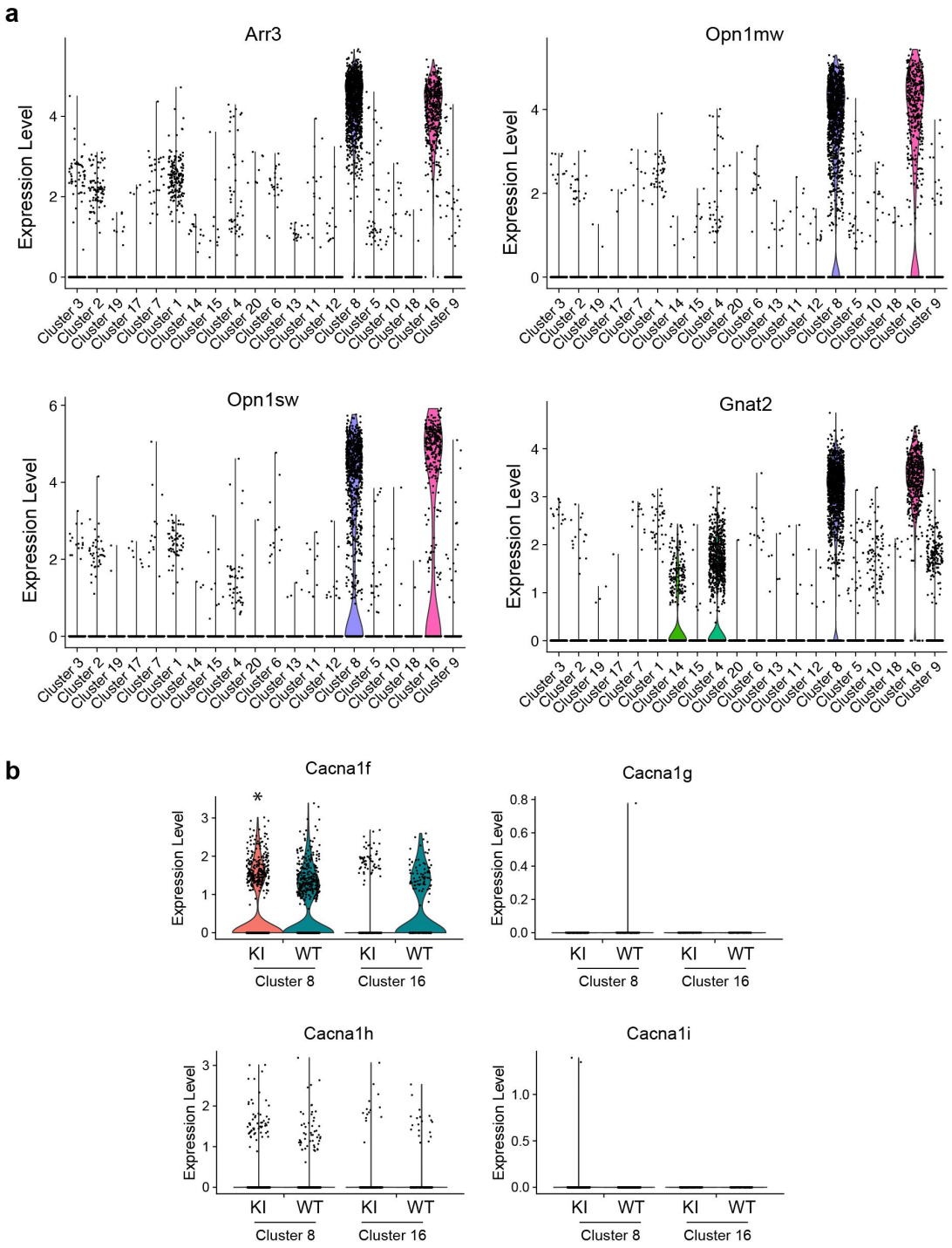

Supplementary Figure S3.

Violin plots showing expression levels of transcripts at the single cell level in the retina of WT and G369i KI mice.

Each point represents result from a single cell. ***a***, Expression levels of transcripts known to be expressed in cones. Cells were grouped according to their transcriptional profiles using unsupervised clustering. Clusters 8 and 16 were identified as cones based on their high expression of Arr3, Opn1mw, Opn1sw, and Gnat2. ***b***, Expression of transcripts that encode Cav1.4 (Cacna1f) and Cav3 subtypes (Cacna1g, Cacna1h, Cacna1i) in clusters 8 and 16 in retina from WT and G369i KI mice. In cluster 8, there was a small but significant decrease in the level of Cacna1f in the G369i KI vs WT (*, p = 0.01) but not in cluster 16 (p =0.09). There was no significant difference in the level of Cacna1h between genotypes in cluster 8 or 16 (p = 1).

References

1. Snellman J., et al. (2011) **Acute destruction of the synaptic ribbon reveals a role for the ribbon in vesicle priming** *Nat Neurosci* **14**:1135–1141

2. Dembla E., Dembla M., Maxeiner S., Schmitz F (2020) **Synaptic ribbons foster active zone stability and illumination-dependent active zone enrichment of RIM2 and Cav1.4 in photoreceptor synapses** *Sci Rep* **10**

3. Haverkamp S., Grunert U., Wassle H (2000) **The cone pedicle, a complex synapse in the retina** *Neuron* **27**:85–95

4. Mercer A.J., Thoreson W.B (2011) **The dynamic architecture of photoreceptor ribbon synapses: cytoskeletal, extracellular matrix, and intramembrane proteins** *Vis Neurosci* **28**:453–471

5. Frederick C.E., Zenisek D (2023) **Ribbon Synapses and Retinal Disease: Review** *Int J Mol Sci* **24**

6. Mansergh F., et al. (2005) **Mutation of the calcium channel gene Cacna1f disrupts calcium signaling, synaptic transmission and cellular organization in mouse retina** *Hum Mol Genet* **14**:3035–3046

7. Liu X., et al. (2013) **Dysregulation of Cav1.4 channels disrupts the maturation of photoreceptor synaptic ribbons in congenital stationary night blindness type 2** *Channels* **7**:514–523

8. Chang B., et al. (2006) **The nob2 mouse, a null mutation in Cacna1f: anatomical and functional abnormalities in the outer retina and their consequences on ganglion cell visual responses** *Vis Neurosci* **23**:11–24

9. Singh A., et al. (2006) **C-terminal modulator controls Ca2+-dependent gating of Cav1.4 L-type Ca2+ channels** *Nat Neurosci* **9**:1108–1116

10. Wahl-Schott C., et al. (2006) **Switching off calcium-dependent inactivation in L-type calcium channels by an autoinhibitory domain** *Proc. Natl. Acad. Sci. U. S. A* **103**:15657–15662

11. Bech-Hansen N.T., et al. (1998) **Loss-of-function mutations in a calcium-channel a1-subunit gene in Xp11.23 cause incomplete X-linked congenital stationary night blindness** *Nature Genet* **19**:264–267

12. Strom T.M., et al. (1998) **An L-type calcium-channel gene mutated in incomplete X-linked congenital stationary night blindness** *Nature Genet* **19**:260–263

13. Waldner D.M., Bech-Hansen N.T., Stell W.K (2018) **Channeling Vision: CaV1.4-A Critical Link in Retinal Signal Transmission** *Biomed Res Int* **2018**

14. Boycott K.M., Pearce W.G., Bech-Hansen N.T (2000) **Clinical variability among patients with incomplete X-linked congenital stationary night blindness and a founder mutation in CACNA1F** *Can J Ophthalmol* **35**:204–213

15. Zeitz C., Robson A.G., Audo I (2015) **Congenital stationary night blindness: an analysis and update of genotype-phenotype correlations and pathogenic mechanisms** *Progress in retinal and eye research* **45**:58–110

16. Regus-Leidig H., et al. (2014) **Photoreceptor degeneration in two mouse models for congenital stationary night blindness type 2** *PLoS One* **9**

17. Zabouri N., Haverkamp S (2013) **Calcium channel-dependent molecular maturation of photoreceptor synapses** *PLoS One* **8**

18. Raven M.A., et al. (2008) **Early afferent signaling in the outer plexiform layer regulates development of horizontal cell morphology** *J Comp Neurol* **506**:745–758

19. Maddox J.W., et al. (2020) **A dual role for Cav1.4 Ca(2+) channels in the molecular and structural organization of the rod photoreceptor synapse** *Elife* **9**

20. Perez-Reyes E (2003) **Molecular physiology of low-voltage-activated t-type calcium channels** *Physiol Rev* **83**:117–161

21. Davison A., Lux U.T., Brandstatter J.H., Babai N (2022) **T-Type Ca(2+) Channels Boost Neurotransmission in Mammalian Cone Photoreceptors** *J. Neurosci* **42**:6325–6343

22. Koschak A., et al. (2003) **Cav1.4alpha1 subunits can form slowly inactivating dihydropyridine-sensitive L-type Ca2+ channels lacking Ca2+-dependent inactivation** *J. Neurosci* **23**:6041–6049

23. Williams B., Maddox J.W., Lee A (2022) **Calcium Channels in Retinal Function and Disease** *Annu Rev Vis Sci*

24. Martemyanov K.A., Sampath A.P (2017) **The Transduction Cascade in Retinal ON-Bipolar Cells: Signal Processing and Disease** *Annu Rev Vis Sci* **3**:25–51

25. Hack I., Frech M., Dick O., Peichl L., Brandstatter J.H (2001) **Heterogeneous distribution of AMPA glutamate receptor subunits at the photoreceptor synapses of rodent retina** *Eur J Neurosci* **13**:15–24

26. Brandstatter J.H., Koulen P., Wassle H (1997) **Selective synaptic distribution of kainate receptor subunits in the two plexiform layers of the rat retina** *J. Neurosci* **17**:9298–9307

27. Feigenspan A., Babai N (2015) **Functional properties of spontaneous excitatory currents and encoding of light/dark transitions in horizontal cells of the mouse retina** *Eur J Neurosci* **42**:2615–2632

28. Krizaj D (2012) **Calcium stores in vertebrate photoreceptors** *Adv Exp Med Biol* **740**:873–889

29. Nusinowitz S., Ridder W.H, Ramirez J. (2007) **Temporal response properties of the primary and secondary rod-signaling pathways in normal and Gnat2 mutant mice** *Exp Eye Res* **84**:1104–1114

30. Vinberg F., Wang T., Molday R.S., Chen J., Kefalov V.J (2015) **A new mouse model for stationary night blindness with mutant Slc24a1 explains the pathophysiology of the associated human disease** *Hum Mol Genet* **24**:5915–5929

31. Bimonte-Nelson H., Daniel J., Koebele S. (2015) **The maze book: theories, practice, and protocols for testing rodent cognition**

32. Beier C., et al. (2017) **Deafferented Adult Rod Bipolar Cells Create New Synapses with Photoreceptors to Restore Vision** *J. Neurosci* **37**:4635–4644

33. Shen N., Wang B., Soto F., Kerschensteiner D (2020) **Homeostatic Plasticity Shapes the Retinal Response to Photoreceptor Degeneration** *Curr Biol* **30**:1916–1926

34. Leinonen H., et al. (2020) **Homeostatic plasticity in the retina is associated with maintenance of night vision during retinal degenerative disease** *Elife* **9**

35. Care R.A., et al. (2020) **Mature Retina Compensates Functionally for Partial Loss of Rod Photoreceptors** *Cell rep* **31**

36. Kiyonaka S., et al. (2007) **RIM1 confers sustained activity and neurotransmitter vesicle anchoring to presynaptic Ca2+ channels** *Nat Neurosci* **10**:691–701

37. Kiyonaka S., et al. (2012) **Physical and functional interaction of the active zone protein CAST/ERC2 and the beta-subunit of the voltage-dependent Ca(2+) channel** *Journal of biochemistry* **152**:149–159

38. tom Dieck S., et al. (2005) **Molecular dissection of the photoreceptor ribbon synapse: physical interaction of Bassoon and RIBEYE is essential for the assembly of the ribbon complex** *J Cell Biol* **168**:825–836

39. Alpadi K., et al. (2008) **RIBEYE recruits Munc119, a mammalian ortholog of the Caenorhabditis elegans protein unc119, to synaptic ribbons of photoreceptor synapses** *J. Biol. Chem* **283**:26461–26467

40. Haeseleer F (2008) **Interaction and colocalization of CaBP4 and Unc119 (MRG4) in photoreceptors** *Invest Ophthalmol Vis Sci* **49**:2366–2375

41. Haeseleer F., et al. (2004) **Essential role of Ca2+-binding protein 4, a Cav1.4 channel regulator, in photoreceptor synaptic function** *Nat Neurosci* **7**:1079–1087

42. Schmitz F., Konigstorfer A., Sudhof T.C (2000) **RIBEYE, a component of synaptic ribbons: a protein's journey through evolution provides insight into synaptic ribbon function** *Neuron* **28**:857–872

43. tom Dieck S., et al. (2012) **Deletion of the presynaptic scaffold CAST reduces active zone size in rod photoreceptors and impairs visual processing** *J. Neurosci* **32**:12192–12203

44. Macosko E.Z., et al. (2015) **Highly Parallel Genome-wide Expression Profiling of Individual Cells Using Nanoliter Droplets** *Cell* **161**:1202–1214

45. Koschak A., et al. (2001) **a1D (Cav1.3) subunits can form L-type Ca2+ channels activating at negative voltages** *J. Biol. Chem* **276**:22100–22106

46. Tringham E., et al. (2012) **T-type calcium channel blockers that attenuate thalamic burst firing and suppress absence seizures** *Sci Transl Med* **4**

47. Cai S., Gomez K., Moutal A., Khanna R (2021) **Targeting T-type/CaV3.2 channels for chronic pain** *Transl Res* **234**:20–30

48. Garcia-Caballero A., et al. (2014) **The deubiquitinating enzyme USP5 modulates neuropathic and inflammatory pain by enhancing Cav3.2 channel activity** *Neuron* **83**:1144–1158

49. Welsby P.J., et al. (2003) **A mechanism for the direct regulation of T-type calcium channels by Ca2+/calmodulin-dependent kinase II** *J. Neurosci* **23**:10116–10121

50. Gomez K., et al. (2020) **Cdk5-Dependent Phosphorylation of Ca(V)3.2 T-Type Channels: Possible Role in Nerve Ligation-Induced Neuropathic Allodynia and the Compound Action Potential in Primary Afferent C Fibers** *J. Neurosci* **40**:283–296

51. Ingram N.T., Sampath A.P., Fain G.L (2019) **Voltage-clamp recordings of light responses from wild-type and mutant mouse cone photoreceptors** *J. Gen. Physiol* **151**:1287–1299

52. Spiwoks-Becker I., Glas M., Lasarzik I., Vollrath L (2004) **Mouse photoreceptor synaptic ribbons lose and regain material in response to illumination changes** *Eur J Neurosci* **19**:1559–1571

53. Regus-Leidig H., Specht D., Tom Dieck S., Brandstatter J.H (2010) **Stability of active zone components at the photoreceptor ribbon complex** *Mol Vis* **16**:2690–2700

54. Sheets L., Kindt K.S., Nicolson T (2012) **Presynaptic CaV1.3 channels regulate synaptic ribbon size and are required for synaptic maintenance in sensory hair cells** *J. Neurosci* **32**:17273–17286

55. Wong H.C., et al. (2019) **Synaptic mitochondria regulate hair-cell synapse size and function** *Elife* **8**

56. Goel P., et al. (2019) **Homeostatic scaling of active zone scaffolds maintains global synaptic strength** *J Cell Biol* **218**:1706–1724

57. Hong H., et al. (2020) **Structural Remodeling of Active Zones Is Associated with Synaptic Homeostasis** *J. Neurosci* **40**:2817–2827

58. Kerov V., et al. (2018) **alpha2delta-4 Is Required for the Molecular and Structural Organization of Rod and Cone Photoreceptor Synapses** *J. Neurosci* **38**:6145–6160

59. Zanetti L., et al. (2021) **Function of cone and cone-related pathways in CaV1.4 IT mice** *Sci Rep* **11**

60. Knoflach D., et al. (2013) **Cav1.4 IT mouse as model for vision impairment in human congenital stationary night blindness type 2** *Channels* **7**:503–513

61. Perez-Reyes E., Van Deusen A.L., Vitko I (2009) **Molecular pharmacology of human Cav3.2 T-type Ca2+ channels: block by antihypertensives, antiarrhythmics, and their analogs** *The Journal of pharmacology and experimental therapeutics* **328**:621–627

62. Choi S.Y., Jackman S., Thoreson W.B., Kramer R.H (2008) **Light regulation of Ca2+ in the cone photoreceptor synaptic terminal** *Vis Neurosci* **25**:693–700

63. Bijveld M.M., et al. (2013) **Assessment of night vision problems in patients with congenital stationary night blindness** *PLoS One* **8**

64. Peloquin J.B., Rehak R., Doering C.J., McRory J.E (2007) **Functional analysis of congenital stationary night blindness type-2 CACNA1F mutations F742C, G1007R, and R1049W** *Neuroscience* **150**:335–345

65. Hoda J.C., Zaghetto F., Koschak A., Striessnig J (2005) **Congenital stationary night blindness type 2 mutations S229P, G369D, L1068P, and W1440X alter channel gating or functional expression of Cav1.4 L-type Ca2+ channels** *J. Neurosci* **25**:252–259

66. Lee A., et al. (2015) **Characterization of Cav1.4 complexes (α11.4, β2, and α2δ–4) in HEK293T cells and in the retina** *J. Biol. Chem* **290**:1505–1521

67. Edelstein A., Amodaj N., Hoover K., Vale R., Stuurman N (2010) **Computer control of microscopes using μManager** *Curr Protoc Mol Biol* **14**

68. Edelstein A.D., et al. (2014) **Advanced methods of microscope control using muManager software** *J Biol Methods* **1**

69. DeVries S.H., Schwartz E.A (1999) **Kainate receptors mediate synaptic transmission between cones and 'Off' bipolar cells in a mammalian retina** *Nature* **397**:157–160

70. Miao Z., Deng K., Wang X., Zhang X (2018) **DEsingle for detecting three types of differential expression in single-cell RNA-seq data** *Bioinformatics* **34**:3223–3224

71. Johnson J.E., et al. (2007) **Spatiotemporal regulation of ATP and Ca2+ dynamics in vertebrate rod and cone ribbon synapses** *Mol Vis* **13**:887–919

72. Schindelin J., et al. (2012) **Fiji: an open-source platform for biological-image analysis** *Nature methods* **9**:676–682

Editors

Reviewing Editor

Nils Brose

Max Planck Institute of Experimental Medicine, GÃ¶ttingen, Germany

Senior Editor

Kenton Swartz

National Institute of Neurological Disorders and Stroke, Bethesda, United States of America

Joint Public Review

Cav1.4 calcium channels control voltage-dependent calcium influx at photoreceptor synapses, and congenital loss of Cav1.4 function causes stationary night blindness CSNB2. Based on a broad portfolio of methodological approaches - genetic mouse models, immunolabeling and microscopic imaging, serial block-face-SEM, ERGs, and electrophysiology - the authors show that cone photoreceptor synapse development is strongly perturbed in the absence of Cav1.4 protein, and that expression of a nonconducting Cav1.4 channel mitigates these perturbations. Further data indicate that Cav3 channels are present, which, according to the authors, may compensate for the loss of Cav1.4 calcium currents and thus maintain cone synaptic transmission. These data, which are in agreement with a similar study by the same authors on rod photoreceptor synapses, help to explain what functional defects exactly cause CSNB2 and why it is accompanied by only mild visual impairment.

The strengths of the present study are its conceptual and experimental soundness, the broad spectrum of cutting-edge methodological approaches pursued, and the convincing differential analysis of mutant phenotypes. Weaknesses mainly concern the mechanism by which Cav3 channels might partially compensate for the loss of Cav1.4 calcium currents.

https://doi.org/10.7554/eLife.94908.2.sa1

Author response:

The following is the authors' response to the original reviews.

> ***Reviewer #1 (Recommendations For The Authors):***
>
> *The authors should perform experiments to answer this question: does Cav3 transcription increase in the G369i-KI, or is there instead some post-transcriptional modulation that permits surface expression of functional Cav3-containing channels in the absence of typical HVA Ca conductances? Also, the authors should determine whether G369i-KI can mediate Ca2+ release from intracellular stores and whether release from stores is upregulated as Cav3-containing channel expression (or function) is increased.*

We performed transcriptomic (drop-seq) analysis to test whether a Cav3 subtype is upregulated in cones of G369i KI mice. These experiments show that, consistent with previous studies (PMID 35803735, 26000488), Cacna1h appears to be the primary Cav3 subtype expressed mouse cones. However, as shown in new Supp.Fig.S3, there was no significant difference in the levels of Cacna1h transcripts in WT and G369i KI cones. Therefore, we propose that there may be some post-transcriptional modification, or alteration in a pathway that regulates channel availability, that enables the contribution Cav3 channels to the whole-cell Ca2+ current in the absence of functional Cav1.4 channels cones.

We also performed Ca2+ imaging experiments in WT vs G369i KI cone terminals to assess whether the diminutive Cav3 current in G369i KI cone terminals may be compensated by upregulation of a Ca2+ signal such as from intracellular stores. Arguing against this possibility, depolarization-evoked Ca2+ signals in G369i KI cones were dramatically reduced compared to WT cones (new Fig.9).

> ***Reviewer #2 (Recommendations For The Authors):***
>
> *Major points-*
>
> *(1) It is stated in too many places that cone features in the Cav1.4 knock-in are "intact", preserved, or spared, but this representation is not accurate. There are two instances in this study that qualify as intact when comparing KI to WT: 1) the photopic a-waves in the Cav1.4 knock-in (also demonstrated in Maddox et al 2020) and 2) latency to the platform (current MS, Figure 7f). However, in the numerous instances listed below, the authors compared the Cav1.4 knock-in to the Cav1.4 knock-out, and then referred to the KI as exhibiting intact responses. The reference point for intactness needs to be wildtype, as appropriately done for Figures 2 and 3, and when comparing the KI to the KO the phrasing should be altered; for example: "the KI was spared from the extensive degeneration witnessed in the KO....".*

In most cases, we clearly note that there are key differences in the WT and the G369i KI cone synapses, which highlight the importance of Cav1.4-specific Ca2+ signals for certain aspects of the cone synapse. We disagree with the reviewer on the point that we did not often use the WT as a reference since most of our experiments involved comparisons of only WT and G369i

KI (Figs. 3-6) or WT, G369i KI, and Cav1.4 KO (Figs.1,7—and in these cases comparisons specifically between WT and G369i KI mice were included). We used “intact” as a descriptor for G369i KI cone synapses since these are actually present, albeit abnormal in the G369i KI retina, whereas cone synapses are completely absent in the Cav1.4 KO retina. To avoid confusion, we modified our use of “intact” and “preserved” where appropriate.

> *A. Abstract, line 34 to 35: ".....preserved in KI but not in KO.".*

Abstract was rewritten and this line was removed.

> *B. Line 36: "....synaptogenesis remains intact". The MS documents many differences in the morphology of KI and WT cones (immunofluorescence and electron microscopy data), which is counter to an intact phenotype.*

The sentence was: “In CSNB2, we propose that Cav3 channels maintain cone synaptic output provided that the Ca2+-independent role of Cav1.4 in cone synaptogenesis remains intact.”

Here the meaning of “intact” refers to the Ca2+ -independent role of Cav1.4, not synapses. Thus, we have left the sentence unchanged.

> *C. This strikes the right balance, lines 67 to 68: "....although greatly impaired.....".*
>
> *D. Line 149, "Cone signaling to a postsynaptic partner is intact in G369i KI mice". This description is inaccurate. Here there is only WT and KI, and the text reads as follows in line 162: "terminals (Figure 6b). The ON and OFF components of EPSCs in G369i KI HCs were measurable, although lower in amplitude than in WT (Figure 6a,b)." Neither "measurable" nor "lower in amplitude" meet the definition of "intact", and actual numerical values are lacking in the text.*

We have added results showing that there are no light responses in the Cav1.4 KO horizontal cells and have modified the sentence to: “Cone synaptic responses are present in horizontal cells of G369i KI but not Cav1.4 KO mice”.

We have modified discussion of these results as (line 210-213): “Consistent with the lack of mature ribbons and abnormal cone pedicles (Fig.1), HC light responses were negligible in Cav1.4 KO mice (Fig.8a,b). In contrast, the ON and OFF responses were present in G369i KI HCs although significantly lower in amplitude than in WT HCs (Fig. 8a,b).”

> *E. Please add a legend to Figure 6a to indicate the intensities. The shape of the KI responses is different from the control which is worthy of discussion: i) there is no clear cessation of HC EPSCs in the KI during the light ON period (when release stops, Im fluctuations should be minimal), and ii) the "peaked" appearances of the initial 500ms of the On and Off periods are very similar in shape for the KI (hard to interpret in the same fashion as a control response). How were the On and Off amplitudes analyzed? Furthermore, the OFF current is not summarized in Figure 6D, but should not this be when Cav3 should be opening and triggering release: Off response-EPSC? Lastly, Figure 6b,d shows a ~70% reduction in On-current in the KI, and the KI example of 6b an 80% reduction in Off current compared to WT. Yet, the only place asterisks are used to indicate sig diff is the DNQX data within each genotype in Fig 6d. These data cannot be described as showing "intact" KI responses, and the absence of numerical and statistical values needs to be addressed.*

New Fig.8a depicting the horizontal cell light responses has been modified to include the legend indicating light intensities. The ON and OFF amplitudes were analyzed as the peak current amplitudes. This information has been added to the legend.

The reviewer is correct in that the OFF response represents the EPSC whereas the ON response represents the decrease in the EPSC with light. To avoid confusion, we changed the y axis label for the averaged data to read ON or OFF “response” rather than “current” in new Fig.8b.

As the reviewer suggests, the more transient nature of the KI response during the light ON period could result from aberrant continuation of vesicular release during the light-induced hyperpolarization of cones in the KI mice, in contrast to the prolonged suppression of release by light which is evident in the WT responses. We speculated on this difference as follows (lines 237-241):

“In addition to its smaller amplitude, the transient nature of the ON response in G369i KI HCs suggested inadequate cessation of cone glutamate release by light (Fig.8b). Slow deactivation of Cav3 channels and/or their activation at negative voltages20 could give rise to Ca2+ signals that support release following light-induced hyperpolarization of G369i KI cones.”

We added astericks to new Fig.8b,d indicating statistical differences and description of the tests in the legend.

> *F. line 168 the section titled "Light responses of bipolar cells and visual behavior is spared in G369i KI but not Cav1.4 KO mice".*

Changed to: “Light responses of bipolar cells and visual behavior are present in G369i KI but not Cav1.4 KO mice”

> *Last sentence of erg results, 189-190: "These results suggest that cone-to-CBC signaling is intact in G369i KI mice.". "Spared and intact" are not accurate descriptions. The ERG data presented here shows massive differences between WT and the KI, except in the instance of awaves.*

This sentence was removed.

> *As for Figure 6, the results text related to Figure 7a-d does not present real numbers for ERG responses, and there is no indication of significant differences there or in the Figure panels. For instance, in Figure 7b, b-waves are KI are comparable to KO, except at the two highest-intensity flashes that show KI responses ~20% the amplitude of WT. Presentation of KI and KO data on a 6- to 10-fold expanded scale higher than WT can be misleading: a quick read of these Figure panels might make one incorrectly conclude that the KI is intact while the KO is impaired when compared to WT. The Methods section needs more details on the ERG analysis (e.g. any filtering out of oscillatory potentials when measuring b-wave, and what was the allowable range of time-to-peak for b-wave amplitude, etc..).*

The vertical scaling of the ERG results in new Fig.10c,d has been changed so as to reflect clearly diminished responses of the KO and KI vs the WT. Further details regarding the ERG analysis was added to the Methods section.

> *G. Can you point to other studies that have used the "visible platform swim test" used in Figure 7e, f, and specify further how mice were dark/light adapted prior to the recordings?*

As referenced in the Methods, original line 674, the methods we used for the swim test were described in our previous study (PMID 29875267). Other studies that have used this assay include PMIDs: 28262416, 26402607.

> *(2) The Maddox et al 2020 study does not safely address whether rods have a residual T-type Ca2+ current in the Cav 1.4 KO or KI. The study showed that membrane currents measured from rods in the KI and KO retina were distinct from WT, supporting their claim that L-type Ca2+ current is absent in the KI and KO. However, the recordings had shortcomings that challenge the analysis of Ca2+ currents: i) collected at room temp (22-24{degree sign}C), ii) at an unknown distance from the terminal (uncertain voltage clamp), iii) with a very slow voltage ramp rate that is not suitable for probing T-type currents (Figure 1d Maddox 2020, 140 mV over 1 sec: 7msec/1mV), and iv) at a signal-to-noise that does not allow to resolve a membrane current under 1 pA (avg wt rod Ca2+ current was -3.5 pA, and line noise ~1pA peak-to-peak in Maddox 2020). Suggestion: say T-type currents were not probed in Maddox et al 2020, but Davison et al 2022 did not find PCR signal for Cav3.2 in rods.*

We disagree that recordings in the Maddox 2020 study were not sufficient to uncover a T-type current. The voltage ramps in that study were not much slower than that of the Davison et al. 2022 study (they used 0.19 mV/ms). Moreover, in new Supp. Fig.S1, we show that like the slower voltage ramp (0.15 mV/ms) used in the prior study of G369i KI rods, the voltage ramps we used in the present study (0.5 mV/ms), which clearly evoke currents with T-type properties in G369i KI cones (Fig.2a,b, Fig.3a,b) do not evoke currents in WT or G369i KI rods.

> *Minor comments.*
>
> *(1) Suggestion: add an overview panel to Figure 1 that shows the rod terminals in the KI. The problem is that cropping out the ribbon and active zone signals from rods, to highlight cones, can give the impression that the cones are partially spared in the KI, and the rods are not spared at all. (yet you nicely clarify this in Figure 4 and in the legend and text, etc.).*

We chose to modify the legend with this information as in Fig.4 rather than modify the figure.

> *(2) Mouse wt cone Ca2+ currents look like L-type currents, as do your monkey and squirrel cone recordings, and also much like those of mouse rods (see Figure S5, Hagiwara et al., 2018 or Grabner and Moser 2021). Your pharm data from mice and squirrels further supports your conclusion, and certainly took much effort. Davison et al 2022 J Neurosci showed PCR results that support their claim that a Cav3 current exists in wt cones. Questions: 1) have you tried PCR? 2) Can you offer more details on what Cav3 KO you tried and what antibodies failed to confirm the KO? As the authors know, one complication is that the deletion of one Cav can be compensated for by the expression of a new Cav. There are 3 types of Cav3s and removal of one type may be compensated for by another Cav3.*

We have included drop-seq data (new Supp.Fig.S3) implicating Cav3.2 as the main Cav3 subtype in cones and have modified our discussion of these results accordingly. These experiments did not reveal any changes in Cav3 subtype expression in G369i KI vs WT cones.

> *(3) Lines 95/96- onward, spend more time telling the story. When working out the biophysical and pharmacological behavior of the Ca2+ currents, you might want to initially refer to the membrane current as a membrane current, and then state how your voltage protocols, intra- and extra-cell solutions, and drugs helped you verify 1) L-type and 2) T-type Ca2+ currents.*

We have modified the text with more detail.

> *(4) If data is in hand, add a ramp I-V to Figure S2, which shows the response of the ground squirrel cone. The steps in S2a are excellent for making your point that a transient current is missing, and the bipolar is a great control to illustrate ML218 works. However, a comparison of a squirrel cone ramp to a bipolar ramp response could complete the figure.*

See Reponse to #5 below.

> *(5) Consider moving Supplementary Figures S2 and S3 to the main text; these are highly relevant to the story, novel, and well-executed.*

Fig.S2 and S3 were added as new Figs.4,5. The new Fig.4 includes voltage ramps in ground squirrel cones (panel a) to compare with the bipolar data (panel f).

> *(6) The nice electron microscopy reconstructions are not elaborated on in any detail, and there is no mention of ribbon size. Is the resolution sufficient to estimate ribbon size, the number of synaptic vesicles around the ribbon and in the adjacent cytosol? The images indicate major changes in the morphology of the terminals. Is the glial envelope similar in WT and KI?*

Since ribbons were quantified extensively in the confocal analyses in Fig.6, we felt it unnecessary to add this to the EM analysis which focused mainly on aspects of 3D structure (i.e., arrangement of ribbons, postsynaptic wiring, cone pedicle morphology). We added further discussion of the change in morphology of the G369i KI cone pedicle (lines 200-203): “Compared to WT, ribbons in G369i KI pedicles appeared disorganized and were often parallel rather than perpendicular to the presynaptic membrane (Fig.7a-c). Consistent with our confocal analyses (Fig.1), G369i KI cone pedicles extended telodendria in multiple directions rather than just apically (Fig. 7a).”

While we did not opt to characterize the glial envelope in WT cones, we did add an analysis of synaptic vesicles around ribbons to Table 2.

> *(7) Discussion line 250: "we found no evidence for a functional contribution of Cav3 in our recordings of cones in WT mice (Figures. 2,3), ground squirrels, or macaque (Supplementary Figures S2 and S3).". I would not use "functional" in this context because when comparing your work to Davison et al 2022, they defined functional as a separate response component driven by Cav3. For instance, they examined the influence of their T-type current on exocytosis (by membrane capacitance) and other features like spiking Ca2+ transients. Suggestion: substitute functional with "detectable", and say "we found no detectable Cav currents". Or if you had Ttype staining, but not T-type Ca2+ currents, then say "no functional current even though there is staining...".*

We have modified the text as (lines 336-338): “However, in contrast to recordings of WT mouse cone pedicles in a previous study21, we found no evidence for Cav3-mediated currents in somatic recordings of cones in WT mice (Figs.2,3).”

We propose an alternative interpretation of the results in the Davison et al study concerning the conclusion that Cav3 channels contribute to Ca2+ spikes and exocytosis. That study used 100 µM Ni2+ to block a “T-type” contribution to spike activity in cones. In their Figs.4,5, the spikes are suppressed by 100 µM Ni2+ and 10 µM nifedipine, a Cav1 antagonist, and spared by the T-type selective drug Z944. This is problematic for several reasons. First, as shown by the authors

(their Fig.2A1,A2) and others (PMID: 15541900), 100 µM Ni2+ inhibits Cav1-type currents in photoreceptors. Second, Z944 potentiates Cav1 current in their mouse cones (their Fig.2C1,C2). Thus, both reagents are suboptimal for dissecting the contribution of either Cav subtype to spiking activity. With respect to Cav3 channels and exocytosis, these authors interpreted a reduction in exocytosis upon holding at -39 mV compared to at -69 mV as indicating a loss of a T-type driven component of release. However, Cav1 channel inactivation (PMID: 12473074) could lead to the observed reduction in exocytosis at -30 mV.

> *(8) Additional literature related to your Intro and Discussion. Regarding CSNB2, related mutations of active zone proteins, and what happens to Ca2+ currents when ribbons are deleted, you might want to consider the following studies that measure Ca2+ currents from rods: conditional KO of RIM1/2 (Grabner et al 2015 JN), KO of ELKS1/2 (Hagiwara et al, 2018 JCB), and KO of Ribeye (Grabner and Moser eLife 2021). In these studies, the Cav currents were absent in rods of the ELKS1/2 DKO, strongly reduced (80%) in the RIM1/2DKO, but altered in more subtle ways (activation-inactivation) without significantly changing steady-state Ca2+ current in the Ribeye KO. This does not seem to support some of the arguments you have made in the Introduction and Discussion regarding ribbon size and Ca2+ currents, yet the suggested literature is related to the topic at hand.*

A description of these synaptic proteins as potential mediators of the effect of Cav1.4 on ribbon morphogenesis was added to the Discussion, lines 325-327.

> *(9) Line 129: "Along with the major constituents of the ribbon, CtBP2, and RIBEYE", for clarity Ribeye has two domains, one that is identical to CtBP2 (B-domain) and the unique Ribeye domain (A-domain) that is only expressed at ribbon synapses. And, Piccolino is also embedded in the ribbon (Brandstaetter lab, Wichmann/Moser labs). In other words, Ribeye and Piccolino are the major constituents of the ribbon.*

To avoid confusion, we simply mention Ctbp2 and RIBEYE in the context of the corresponding antibodies that were used to label ribbons.

> *(10) Abstract: consider to rephrase "Ca2+-independent role of Cav1.4" by "Ca2+-permeationindependent role of Cav1.4" or alike*

Sentence changed to: “In CSNB2, we propose that Cav3 channels maintain cone synaptic output provided that the nonconducting role of Cav1.4 in cone synaptogenesis remains intact.”

> ***Reviewer #3 (Recommendations For The Authors):***
>
> *Cav1.4 voltage-gated calcium channels play an important role in neurotransmission at mammalian photoreceptor synapses. Mutations in the CACNA1f gene lead to congenital stationary night blindness that particularly affects the rod pathway. Mouse Cav1.4 knockout and Cav1.4 knockin models suggest that Cav1.4 is also important for the cone pathway. Deletion of Cav1.4 in the knockout models leads to signaling malfunctions and to abundant morphological re-arrangements of the synapse suggesting that the channel not only has a role in the influx of Ca2+ but also in the morphological organization of the photoreceptor synapse. Of note, also additional Cav-channels have been previously detected in cone synapses by different groups, including L-type Cav1.3 (Wu et al., 2007; pmid; Kersten et al., 2020; pmid), and also T-type Cav3.2 (Davison et al., 2021; pmid 35803735).*

> *In order to study a conductivity-independent role of Cav1.4 in the morphological organization of photoreceptor synapses, the authors generated the knockin (KI) mouse Cav1.4 G369i in a previous study (Maddox et al., eLife 2020; pmid 32940604). The Cav1.4 G369i KI channel no longer works as a Ca2+-conducting channel due to the insertion of a glycine in the pore-forming unit (Madox et al. elife 2020; pmid 32940604). In this previous study (Madox et al. elife 2020; pmid 32940604), the authors analyzed Cav1.4 G369i in rod photoreceptor synapses. In the present study, the authors analyzed cone synapses in this KI mouse.*
>
> *For this purpose, the authors performed a comprehensive set of experimental methods*
>
> *including immunohistochemistry with antibodies (also with quantitative analyses), electrophysiological measurements of presynaptic Ca2+ currents from cone photoreceptors in the presence/absence of inhibitors of L-type- and T-type- calcium channels, electron microscopy (FIB-SEM), ERG recordings and visual behavior tests of the Cav G369i KI in comparison to the Cav1.4 knockout and wild-type control mice.*
>
> *The authors found that the non-conducting Cav channel is properly localized in cone synapses and demonstrated that there are no gross morphological alterations (e.g., sprouting of postsynaptic components that are typically observed in the Cav1.4 knockout). These findings demonstrate that cone synaptogenesis relies on the presence of Cav1.4 protein but not on its Ca2+ conductivity. This result, obtained at cone synapses in the present study, is similar to the previously reported results observed for rod synapses (Maddox et al., eLife 2020, pmid 32940604). No further mechanistic insights or molecular mechanisms were provided that demonstrated how the presence of the Cav channels could orchestrate the building of the cone synapse.*

We respectfully disagree regarding the mechanistic advance of our study. As indicated by Reviewer 2, a major advance of our study is in providing a mechanism that can explain the longstanding conundrum that congenital stationary night blindness type 2 mutations that would be expected to severely compromise Cav1.4 function do not produce complete blindness. Our study provides an important contrast to the Maddox et al 2020 study in showing that rods and cones respond differentially to loss of Cav1.4 function, which is also relevant to the visual phenotypes of CSNB2. How the presence of Cav1.4 orchestrates cone synaptogenesis is an important topic that is outside the scope of our present study.

> *In the present study, the authors also propose a homeostatic switch from L-type to (newly occurring) T-type calcium channels in the Cav1.4 G369i KI mouse as a consequence of the deficient calcium channel conductivity in the Cav1.4 G369i Cav1.4 KI mouse. In cones of the Cav1.4 G369i, the high-voltage activated, L-type Ca2+-entry was abolished, in agreement with their previous paper (Maddox et al., eLife 2020, pmid 32940604). The authors found a lowvoltage activated Ca2+ current instead that they assigned to T-type Ca2+-currents based on pharmacological inhibitor experiments. T-type Ca2+-currents/channels were already previously identified in other studies by independent groups and independent techniques*
>
> *(electrophysiology, RT-PCR, single-cell sequencing) in cones of wild-type mice (Davison et al.,*
>
> *2021, pmid 35803735; Macosko et al., 2015, pmid 26000488; Williams et al., 2022, pmid 35650675). In the present manuscript (Figures 3a/b), the authors also observed a low-voltage activated, T-type like current in cones of wild-type mice, that is isradipine-resistant and affected by the T-type inhibitor ML218. This finding appears compatible with a T-type-like current in wildtype cones and is consistent with the published data*

> *mentioned above, although the authors interpret this data in a different way in the discussion.*
>
> *Due to the noise inherent in whole cell voltage clamp measurements and some crossover effects in the pharmacology, we cannot completely exclude the presence of a T-type current in WT mouse cones. However, our results very clearly support a conclusion opposite to that stated by the reviewer. Namely, if WT mouse cones have T-type Ca currents, then they are far smaller than those in the Cav1.4 G369i KI and KO cones. In particular, while we identified message for Cav3.2 in WT mouse cones, we were unable to identify a functional T-type current by either voltage clamp measurements or pharmacology. See below for a detailed rebuttal.*
>
> *This proposal of a homeostatic switch is not convincingly supported in this reviewer's opinion*
>
> *(for further details, please see below). Furthermore, no data on possible molecular mechanisms were provided that would support such a proposal of a homeostatic switch of calcium channels. No mechanistic/molecular insights were provided for a proposed homeostatic switch between Ltype to T-type channels that the authors propose to occur between wild-type and Cav1.4 G369i as a consequence of conduction-deficient Cav1.4 G369i channels. Is this e.g. based on posttranslational modifications that switch on T-type channels or regulation at the transcriptional level inducing expression of T-type calcium channel or on other mechanisms? The authors remain descriptive with their central hypotheses. No molecular mechanisms/signaling pathways were provided that would support the idea of such a homeostatic switch.*

Homeostatic plasticity refers to the maintenance of neuronal function in response to some perturbation in neuronal activity and can result from changes in the expression of ion channel genes (PMID: 36377048, 32747440, 19778903) or regulatory pathways that modulate ion channels (PMID: 15051886, 32492405). We present multiple lines of evidence showing that Cav3 currents appear in cones upon genetically induced Cav1.4 loss of function and can support cone synaptic responses and visual behavior if cone synapse structure is maintained. Our new transcriptomic studies show no difference between levels of Cav3 channel transcripts in WT and G369i KI cones, suggesting that the appearance of the Cav3 currents in G369i KI cones does not result from an increase in Cav3 gene expression. We are currently investigating our transcriptomic dataset to determine if Cav3 regulatory pathways are upregulated in G369i KI cones and will present this in a follow-up study.

> *The authors show residual photopic signaling in the non-conducting Cav1.4 G369i KI mouse as judged by the recording of postsynaptic currents, ERG recordings and visual behavior tests though in a reduced manner. The residual cone-based signaling could be based on the nonaffected T-type Ca2+ channel conductivity in cone synapses. Given that the L-type current through Cav1.4 is gone in the Cav1.4 G369i KI as previously shown (Maddox et al., 2020, pmid 32940604), the T-type calcium current will remain. However as discussed above, this does not necessarily support the idea of a homeostatic switch.*

A major point which we highlighted with new results is that despite the expression of Cav3 transcripts in WT mouse cones, Cav3 channels do not contribute to the cone Ca2+ current. This is at odds with the Davison et al study (PMID: 35803735, see our response to Reviewer 2, pt 7 for caveats of this study), but our results convincingly show that the Cav3 current appears only when Cav1.4 is genetically inactivated. Pharmacological or electrophysiological methods that should reveal the presence of Cav3 currents do not change the properties of the Ca2+ current in cones of WT mice, ground squirrel, or macaque:

• Figs.2-4: Voltage steps to -40 mV (Fig 2e) that activate a sizeable T-current in G369i KI mouse cones produce a negligible transient at pulse onset in WT mouse cones. Similarly, transient currents that are obvious in G369i KI mouse cones during the final step to -30 mV are absent in WT cones. When we block Cav1.4 with isradipine either in cones of WT mice or ground squirrel, the current that remains does not resemble a Cav3 current but rather a scaled down version of the L-type current. ML218, which readily blocks Cav3 channels in HEK293T cells and in G369i KI cones, has only minor effects in cones of WT mice and ground squirrel; these effects of ML218 can be attributed to non-specific actions on Cav1.4 (new Supp.Fig.S2). New Fig.4 (moved from the supplementary data to the main article) clearly shows that the ML218-sensitive current in ground squirrel cones exhibits properties of Cav1.4 not Cav3 channels.

• Figs.2,5: Holding voltages that inactivate Cav3 channels have no effect on the Ca2+ current in cones of WT mice or macaque (recordings of macaque cones were moved from the supplement to the main article as new Fig.5).

> *In Figure 4 the authors measured an increase in the size of the active zone (as judged by the size of the bassoon cluster) and of the synaptic ribbons in the Cav1.4 G369i. A mechanistic explanation for this phenomenon was not provided and the underlying molecular mechanisms were not unraveled.*
>
> *The FIB-SEM data uncover some ultrastructural alteration/misalignments of the synaptic ribbons and misalignments of the regular arrangement of the postsynaptic dendrites in the G369i KI mice. Also concerning this observation, the study remains descriptive and does not reveal the underlying mechanisms as it would be expected for eLife.*

We respectfully disagree on the descriptive nature of our study and the need for a full characterization of the molecular mechanism underlying the cone synaptic defects in the G369i KI mouse.

> *An important study in the field (Zanetti et al., Sci. Rep. 2021; pmid 33526839) should be also cited that used a gain-of-function mutation of Cav1.4 to analyze its functional and structural role in the cone pathway.*

We have added citation of this paper to the Discussion (lines 354-356).

> *In conclusion, the study has been expertly performed but remains descriptive without deciphering the underlying molecular mechanisms of the observed phenomena, including the proposed homeostatic switch of synaptic calcium channels. Furthermore, a relevant part of the data in the present paper (presence of T-type calcium channels in cone photoreceptors) has already been identified/presented by previous studies of different groups (Macosko et al., 2015; pmid 26000488; Davison et al., 2021; pmid 35803735; Williams et al., 2022; pmid 35650675). The degree of novelty of the present paper thus appears limited. I think that the study might be better suited in a more specialized journal than eLife.*

We thank the reviewer for acknowledging the rigor of our study but disagree with their evaluation regarding the novelty of our work as outlined in our responses above.

https://doi.org/10.7554/eLife.94908.2.sa0